

## MIT Open Access Articles

### *Design of Flat-Plate Dehumidifiers for Humidification– Dehumidification Desalination Systems*

The MIT Faculty has made this article openly available. **Please share** how this access benefits you. Your story matters.

**Citation:** Sievers, Martin, and John H. Lienhard. “Design of Flat-Plate Dehumidifiers for Humidification–Dehumidification Desalination Systems.” *Heat Transfer Engineering* 34, no. 7 (January 2013): 543–561.

**As Published:** <http://dx.doi.org/10.1080/01457632.2013.730355>

**Publisher:** Taylor & Francis

**Persistent URL:** <http://hdl.handle.net/1721.1/86323>

**Version:** Author's final manuscript: final author's manuscript post peer review, without publisher's formatting or copy editing

**Terms of use:** Creative Commons Attribution-Noncommercial-Share Alike



# Design of Flat-Plate Dehumidifiers for Humidification- Dehumidification Desalination Systems

Martin Sievers<sup>1,2</sup> and John H. Lienhard V<sup>1,\*</sup>

<sup>1</sup> Department of Mechanical Engineering, Massachusetts Institute of Technology, Cambridge, MA 02139-4307, USA

<sup>2</sup> Present Address: Institute of Aerospace Thermodynamics (ITLR), Stuttgart University, Pfaffenwaldring 31, 70569, Stuttgart, Germany

## ABSTRACT

Flat-plate heat exchangers are examined for use as dehumidifiers in humidification-dehumidification (HDH) desalination systems. The temperature and humidity ratio differences that drive mass transfer are considerably higher than in air-conditioning systems, making current air-conditioning dehumidifier designs and design software ill-suited to HDH desalination applications. In this work a numerical dehumidifier model is developed and validated against experimental data. The model uses a logarithmic mass transfer driving force and an accurate Lewis number. The heat exchanger is subdivided into many cells for high accuracy. The Ackermann correction takes into account the effect of non-condensable gases on heat transfer during condensation. The influence of various heat exchanger design parameters is thoroughly investigated and suitable geometries are identified. Amongst others, the relationship between heat flow, pressure drop and heat transfer area is shown. The thermal resistance of the condensate layer is negligible for the investigated geometries and operating point. A particle embedded polymer as a flat-plate heat exchanger material for seawater operation substantially improves the heat flux relative to pure polymers and approaches the performance of titanium alloys. Thus, the use of particle embedded polymers is recommended. The dehumidifier model can be applied in design and optimization of HDH desalination systems.

---

\* Corresponding author, Tel. +1-617-253-3790; email: [lienhard@mit.edu](mailto:lienhard@mit.edu)

## INTRODUCTION

The provision of clean water has long been one of the core challenges facing humanity [1]. One way to address the ever-increasing demand for clean water is to desalinate seawater or brackish water, for example, by the humidification-dehumidification (HDH) process. Remarkable improvements in the development of HDH desalination systems have been achieved in recent years [2-8]. However, most improvements have concentrated on new system configurations, thermodynamic analysis, and proof of concept experiments. Solar heaters [6] and humidifiers [7] are the HDH desalination system components which have been investigated in most detail. Dehumidifiers, on the other hand, have often been adapted from existing air conditioning technology, rather than developed in the HDH context. To enable an improved HDH desalination system configuration, an intensive study on dehumidifiers for HDH desalination systems has been performed [9].

A detailed description of HDH desalination systems is given by Narayan et al. [3]. Figure 1 shows a closed-air open-water (CAOW) water-heated HDH desalination system. The main components are a humidifier, a dehumidifier, and a heater. Essentially, the process mimics the rain cycle: warm seawater is evaporated into an air stream in the humidifier. In the ideal case, the air exiting at the top of the humidifier is saturated. It is transferred to the dehumidifier, where it is cooled by cold seawater. The humidity of the saturated air decreases with decreasing temperature in the dehumidifier, so part of the water vapor condenses, producing pure liquid water which is collected in a basin at the bottom of the dehumidifier. This product water can be used in external applications. In a closed-air system, the dehumidified air is recirculated to the humidifier. Latent and sensible heat load are transferred from the air to the seawater side to preheat the seawater. In this water-heated cycle, the preheated seawater is heated further by a solar water heater, before being sprayed into the humidifier. The seawater not vaporized in the humidifier is discarded.

Many variations of this basic architecture exist. The energy input to the system can be transferred to the water flow or to the air flow at different positions. Cycles with pressure variation or extraction of seawater or humid air from the heat exchangers are another field of current research [2].

Previous HDH cycle optimization studies [2-4] are used here to establish the desired inlet and outlet conditions for the dehumidifier. Suitable dehumidifier designs are investigated by means of numerical simulations.

## **Heat Exchangers for Dehumidification**

Different types of heat exchangers have been used as dehumidifiers in HDH desalination systems. The majority of the reviewed articles [3] used plate-fin tube heat exchangers. These have proven to be the most economical heat exchanger for dehumidification in HVAC and are therefore often adapted for HDH processes. Other dehumidifiers found in HDH desalination systems are direct contact, shell and tube, shell and plate, and plate heat exchangers. Usually, plate heat exchangers are less economical but they are highly compact. Plate heat exchangers with flat plates are examined in this publication.

## **Plate Heat Exchangers**

Gasket plate heat exchangers, the most common type of plate heat exchangers, consist of a number of thin plates with a corrugated surface. Gaskets are used to separate and seal the fluids between the plates from each other and to achieve a closed system towards the environment. Chevron (sometimes called herringbone) plates are the most common. For particle embedded polypropylene (PP) plates, which are examined here, corrugated geometries seem less practicable. Flat plates are therefore analyzed here. The seawater is distributed to the plates at the bottom of the heat exchanger by a port manifold, flows upwards and is collected by another manifold header in Z arrangement at the top of the plates. The moist air enters the plate heat exchanger at the top and flows countercurrently between the other plate spaces downwards to the bottom.

In refrigeration systems, plate heat exchangers are preferred to plate-fin tube heat exchangers if the available space is a limiting factor, if the heat exchanger surfaces have to be cleaned, or if the heat exchanger shape is restricted by special geometric constraints. If these conditions do not apply, plate-fin tube heat exchangers are preferred because of their lower production costs per heat exchanger area [10]. With the use of a different plate material, this common industrial practice has to be re-evaluated.

Shell and plate heat exchangers are a hybrid design combining the advantages of plate heat exchangers with those of shell and tube heat exchangers: They have the high mechanical integrity of shell and tube heat exchangers and the superior heat transfer characteristics of plate heat exchangers. The air flow distribution on the shell side results in a lower air-side pressure drop [11]. The first commercial HDH desalination systems designed by Müller-Holst [12, 13] have used a shell and plate dehumidifier.

## **Heat Exchanger Materials**

In industrial practice, plate heat exchangers made of titanium alloy are often used in applications with seawater or brackish water [14] despite the high price. A typical titanium alloy contains 13.5 mass-% Al, 13.3 mass-% V and 10.0 mass-% Cr, and has a thermal conductivity of 21.9 W/(m K).

In the pharmaceutical and chemical industry, graphite heat exchangers are employed in special applications for corrosive fluids. The mixture of graphite particles and epoxy resin has a high thermal conductivity of 125 W/(m K) [15]. However graphite heat exchangers are economically unattractive for HDH desalination.

As an alternative, polypropylene (PP) can be employed in plate heat exchangers [12, 13]. Its characteristics largely differ from those of the previously mentioned materials: It has a high corrosion resistance and a low thermal conductivity of 0.22 W/(m K) [16] combined with a low price. If the low thermal conductivity does not result in a considerable heat flux reduction, PP has a high potential for the application in dehumidifiers of HDH desalination systems. For a plate heat exchanger, the PP wall thickness is of the order of 2 mm; with special treatment 0.7 mm is possible [12]. In this study, the effect on heat exchanger performance of using a polymer instead of a metal is evaluated. If the size of the heat exchanger is not confined, it may be economical to build a larger heat exchanger made of PP rather than a smaller metal heat exchanger. The increased pressure drop and operating costs of a larger heat exchanger have to be evaluated on a case-by-case basis. One challenge resulting from the use of PP in heat exchangers is its comparably high thermal expansion coefficient, which is about an order of magnitude higher than that of a titanium alloy [16, 17]. This places a lower limit on the

plate spacing. In the heat exchanger designed by Müller-Holst [12], this limit is at 10 mm; for a comparable Cu plate heat exchanger, the minimum plate spacing is 4 mm.

One promising method of improving the thermal and mechanical properties of PP is to embed particles within the material. In this way the thermal conductivity can be increased by an order of magnitude, depending on the type and quantity of particles used [18]. Particle fractions of up to 70 vol.-% can be injected during the common extrusion process where the PP is heated up and melted [19]. Other steps of the manufacturing process remain unchanged, as the composite material can be handled in the same way as PP without particles. Thus the material price is approximately the sum of the prices for PP and the particles. Among the analyzed filling materials, copper (Cu) and magnetite ( $\text{Al}_3\text{O}_4$ ) lead to the largest increase in thermal conductivity: to about 2.5 W/(m K) for 35 vol.-% Cu particles, and to about 1.0 W/(m K) for 30 vol.-% magnetite particles [18]. If metal particles are mixed into polymers, an antioxidant and other additives must be introduced during the production process to prevent the metallic ions from oxidizing the polymer chains, which can lead to material failure [20]. Lifetimes of 10 years are attainable [19]. If better mechanical properties are required, a polymer with a higher glass transition temperature should be selected.

Particles at the surface are typically coated with PP after production. This prevents oxidation of the metal particles and contamination of seawater or product water with these particles. Just as in pure PP heat exchangers, the material has a very high corrosion resistance, and the smooth surface reduces particle deposition on the wall. In addition, the density of particle filled PP is lower than that of metals.

## **Heat Exchanger Fouling**

Another issue which is of importance when using seawater, especially at elevated temperature, is fouling on the seawater side of the heat exchanger. Dissolved or suspended solids can deposit on the heat exchanger surface or biofilms develop and build a layer that adds to the heat transfer resistance between air and seawater side. To ensure smooth operation, a pretreatment of the seawater is necessary before it enters the heat exchanger. The fouling resistance depends on different parameters such as seawater flow velocity, surface properties, and temperature. Although the fouling resistance changes

over time, constant values are recommended for the design in the literature [21]. A fouling resistance of  $R_f = 0.043 \text{ m}^2\text{K/kW}$  for seawater operated plate heat exchangers near the coast [21] is used on the seawater side.

## **DEHUMIDIFIER MODEL**

A mathematical model is developed for detailed analysis of the dehumidifier. The fundamental physical basis and the resulting equations used for that model are presented. The cell method [22] is applied. In contrast to standard two zone models [23 - 25], the heat exchanger is not only subdivided into one dry and one wet section, but is discretized into a large number of cells to obtain a more accurate solution. The air and the water outlet states are determined for given air and seawater inlet conditions and heat exchanger geometry.

The model incorporates the following assumptions and features:

- The heat and mass transfer are under steady-state conditions
- The mass transfer is determined by a heat and mass transfer analogy
- The Lewis number,  $Le = 0.865$ , may accurately be applied for HDH operating conditions
- The logarithmic mass transfer driving force is not linearized
- The surface area of a cell is either fully dry or fully wet
- The effect of the condensation induced fluid motion perpendicular to the main air flow direction is accounted for
- The condensate forms a film on the heat exchanger surface. Its thermal conductive resistance is accounted for
- The energy balance includes the temperature change of the condensate in each cell
- The velocity reduction due to condensation is accounted for
- The heat conduction in the plates is one dimensional from the air side to the seawater side
- The heat exchanger is adiabatic towards the ambient
- The heat transfer and the pressure drop are calculated successively

## Derivation of Governing Equations for the Wet Control Volume

Figure 2 (top) shows the one-dimensional discretization of the plate heat exchanger in the  $z$  direction. Figure 2 (below) illustrates an enlarged view of the wet control volume (cell) with the used variables. On the left-hand side seawater flowing upwards is heated. On the right-hand side humid air and condensate flowing countercurrently downwards are cooled and part of the water vapor condenses. During this process the mass flow of dry air remains unchanged, whereas the amount of humid air and condensate change. Heat and mass transfer are simulated at constant pressure and are not coupled to the pressure drop calculation. Both calculations are performed successively, as the pressure drop is small relative to the total pressure.

Liquid water is produced by the condensation of water vapor

$$d\dot{m}_{pw} = -\dot{m}_{da}d\omega. \quad (1)$$

This mass flow of water vapor transports the enthalpy flow  $d\dot{m}_{pw}h_{wg}(T_I)$  in the air to the interfacial boundary I, where  $h_{wg}(T_I)$  is the specific enthalpy of saturated water vapor at the interface temperature  $T_I$ . Additionally, a convective (sensible) heat flow  $d\dot{Q}_I$  is transferred in the negative  $y$ -direction to the air side of the interfacial boundary. Both energy flows reduce the enthalpy flow of the humid air (air energy balance)

$$-\dot{m}_{da}dh_a = d\dot{Q}_I + d\dot{m}_{pw}h_{wg}(T_I) \quad (2)$$

and are transferred through the interfacial boundary to the product water.

Part of this energy flow changes the product water enthalpy flow and the remainder is transferred as a heat flow  $d\dot{Q}$  from the product water to the plate (product water energy balance)

$$d\dot{Q}_I + d\dot{m}_{pw}h_{wg}(T_I) = d(\dot{m}_{pw}h_{pw}) + d\dot{Q}. \quad (3)$$

Combining Eqs. (2) and (3) leads to

$$-d\dot{Q} = \dot{m}_{da}dh_a + d(\dot{m}_{pw}h_{pw}) = \dot{m}_{da}dh_a + \dot{m}_{pw}dh_{pw} + h_{pw}d\dot{m}_{pw}. \quad (4)$$

Neglecting the heat conduction in the plate in  $z$  direction the heat flow  $d\dot{Q}$  is transferred to the seawater side (seawater energy balance)



$$d\dot{Q} = \dot{m}_{sw} dh_{sw}. \quad (5)$$

The differential changes of the specific enthalpy of humid air without condensate ( $\omega \leq \omega_{sat}$ )

$$dh_a = (c_{pda} + \omega c_{pwg})dT + [h_{fg}(T_0) + c_{pwg}(T - T_0)]d\omega \quad (6)$$

and of humid air with condensate ( $\omega > \omega_{sat}$ )

$$dh_a = \left[ c_{pda} + \omega_{sat} c_{pwg} + (\omega - \omega_{sat})c_{pwf} + h_{fg}(T) \frac{\partial \omega_{sat}}{\partial T} \right] dT + c_{pwf}(T - T_0)d\omega \quad (7)$$

are applied to isobaric processes, where  $T$  is the thermodynamic air temperature and  $T_0 = 273.16$  K the thermodynamic reference temperature.

The differential change of the specific enthalpy of product water  $dh_{pw}$  and of seawater  $dh_{sw}$  are related to the changes of the product water temperature  $dt_{pw}$  and of the seawater temperature  $dt_{sw}$  by the specific heat capacity at constant pressure.

The heat flow  $d\dot{Q}_I$  transferred in the air from the bulk flow to the interfacial boundary (condensate) is

$$d\dot{Q}_I = h_{ta}^*(T_\infty - T_I)dA. \quad (8)$$

The heat transfer coefficient  $h_{ta}^*$  includes the effect of non-condensable gases on sensible heat transfer.

When condensation occurs at a surface, the condensed matter is transferred to the condensate film, which acts as a porous surface with suction. This suction causes a velocity normal to the surface, the major source for the difference between dry and wet surface heat transfer coefficients [26-28]. The effect on heat transfer is taken into account by the Ackermann correction [29], which is also known as the stagnant film model of heat transfer at high mass transfer rates [30]. Using the heat transfer coefficient  $h_{ta}$  for the dry case without suction and without condensation from Table 1, the modified heat transfer coefficient in the humid air with suction and with condensation can be determined

$$h_{ta}^* = h_{ta} \zeta, \quad (9)$$

with the correction factor

$$\zeta = \frac{-\Phi}{\exp(-\Phi)-1} \quad \text{where } \Phi = \frac{|\dot{m}_{pw}| c_{pa}}{dA h_{ta}}. \quad (10)$$

This heat transfer coefficient  $h_{ta}^*$  for a wet surface is slightly higher than  $h_{ta}$  for a dry surface. In the current simulations a maximum increase of about 30 % was calculated.

A heat and mass transfer analogy is applied to link the mass transfer to the heat transfer. In terms of the boundary layer theory, the ratio of the Nusselt number and the Sherwood number is:

$$\frac{Sh}{Nu} = \frac{h_{ma} k_a}{h_{ta} D_{wa}} = \frac{C Re^n Sc^m}{C Re^n Pr^m} = \left(\frac{Sc}{Pr}\right)^m = \left(\frac{\alpha_a}{D_{wa}}\right)^m = Le^m. \quad (11)$$

Here,  $Le$  is the Lewis number. Equation (11) has been confirmed experimentally for dehumidification of air by Eckels and Rabas [28].

The mass transfer coefficient  $h_{ma}$  can be calculated from the heat transfer coefficient

$$h_{ma} = \frac{h_{ta} D_{wa}}{k_a} Le^m = \frac{h_{ta}}{\rho_a c_{pa}} Le^{m-1}, \quad (12)$$

where  $m$  is the exponent of the Prandtl number in the heat transfer correlation in Eq. (11). For laminar boundary layer flow,  $m = 1/3$  [30]; in other cases, an appropriate value may be fitted to data.

Poppe [31] uses the constant value  $Le = 0.865$  for air-water cooling tower applications, which is accurate for the operating temperature and pressure range of HDH desalination systems, as well [9].

The solubility of air in the condensed water is negligible, so only the mass transfer of water from the humid air through the interfacial boundary to the condensed water is taken into account. The water vapor is transported in the humid air by diffusion and convection normal to the interfacial boundary. The condensation of water from the humid air may be regarded as diffusion through a semipermeable plane [32]. In this case, the mass transfer rate (in the negative  $y$ -direction in Fig. 2) is

$$d\dot{m}_{pw} = M_w \frac{c D_{wa}}{1-x_w} \frac{dx_w}{dy} dA. \quad (13)$$

For a small water mole fraction  $x_w$  in the humid air ( $x_w \ll 1$ ), the convective mass transport normal to the interfacial boundary would be negligible, i.e., the denominator  $1 - x_w \approx 1$  in Eq. (13). However, at a pressure of 50 kPa, a temperature of 60 °C and a relative humidity of 0.9 as in the dehumidifier,  $x_w = 0.36$  results, which cannot be neglected.

From the film theory, assuming non-zero mass transfer in a thin film of thickness  $\delta$  in the air near the interfacial boundary, the condensate production rate is [30, 32]

$$d\dot{m}_{pw} = M_w \frac{c D_{wa}}{\delta} \ln \frac{1 - x_{w\infty}}{1 - x_{wI}} dA, \quad (14)$$

where  $x_{w\infty}$  and  $x_{wI}$  are the water mole fractions in the air bulk flow and at the air side of the interfacial boundary. By introducing the humidity ratio

$$\omega = \frac{m_w}{m_{da}} = \frac{M_w}{M_{da}} \frac{x_w}{x_{da}} = \frac{M_w}{M_{da}} \frac{x_w}{1 - x_w} = 0.622 \frac{x_w}{1 - x_w} = 0.622 \frac{p_w}{p - p_w} \quad (15)$$

and the mass transfer coefficient  $h_{ma} = D_{wa}/\delta$  for vanishing convective mass flow at the interfacial boundary, and replacing the molar concentration  $c$  of the humid air by the density  $\rho_a$  and the molar mass  $M_a$  of the humid air, and using the heat and mass transfer analogy from Eq. (12) with the thermophysical properties of humid air, Eq. (14) becomes

$$d\dot{m}_{pw} = \frac{h_{ta}}{c_{pa}} \frac{M_w}{M_a} Le^{m-1} \ln \frac{1 - \frac{\omega_\infty}{0.622}}{1 - \frac{\omega_I}{0.622}} dA. \quad (16)$$

The air-side energy balance Eq. (2) is transformed with Eqs. (8), (9), and (16):

$$-\dot{m}_{da} dh_a = h_{ta} \zeta (T_\infty - t_I) dA + h_{wg}(t_I) \frac{h_{ta}}{c_{pa}} \frac{M_w}{M_a} Le^{m-1} \ln \frac{1 - \frac{\omega_\infty}{0.622}}{1 - \frac{\omega_I}{0.622}} dA. \quad (17)$$

The heat flow from the humid air to the seawater must pass through the condensate film. The energy balance for the condensate film (cf. Fig. 2) is

$$h_{tpw}(t_I - t_0) dA + d(\dot{m}_{pw} h_{pw}) = h_{ta} \zeta (T_\infty - t_I) dA + h_{wg}(t_I) \frac{h_{ta}}{c_{pa}} \frac{M_w}{M_a} Le^{m-1} \ln \frac{1 - \frac{\omega_\infty}{0.622}}{1 - \frac{\omega_I}{0.622}} dA,$$

(18)

where  $h_{tpw}$  is the heat transfer coefficient in the condensate film to the plate surface. After the water vapor has passed the interfacial boundary it condenses, changing its specific enthalpy by the specific heat of vaporization  $h_{fg}(t_I)$ . The unknown plate surface temperature  $t_0$  on the condensation side is replaced by the heat flow  $d\dot{Q}$  from the condensate-side plate surface to the seawater bulk flow (cf. Fig. 2). Thus the implicit formula to determine the temperature at the interfacial boundary results

$$t_I = t_{sw} + \frac{d\dot{Q}}{dA} \left( \frac{d_p}{k_p} + \frac{1}{h_{tsw}} \right) + \frac{h_{ta}}{h_{tpw}} \left( \zeta (T_\infty - t_I) + \frac{h_{wg}(t_I) M_w}{c_{pa} M_a} Le^{m-1} \ln \frac{1 - \frac{\omega_\infty}{0.622}}{1 - \frac{\omega_I}{0.622}} \right) - \frac{d(\dot{m}_{pw} h_{pw})}{h_{tpw} dA}, \quad (19)$$

which is solved by iteration together with the other governing equations.

The mean condensate temperature  $t_{pw}$  is related to the condensate temperature  $t_I$  at the interfacial boundary and to the wall temperature  $t_0$  on the condensate side for a laminar condensate film (as in the present system) according to Sadasivan and Lienhard [33]

$$t_{pw} = t_I + \left( 0.683 - \frac{0.228}{Pr} \right) (t_0 - t_I) = t_I + \left( 0.683 - \frac{0.228}{Pr} \right) \left( t_{sw} - t_I + \frac{d\dot{Q}}{dA} \left( \frac{d_p}{k_p} + \frac{1}{h_{tsw}} \right) \right). \quad (20)$$

## Governing Equations and Thermophysical Properties

The seven equations (1), (4), (5), (16), (17), (19) and (20) provide the governing equations for the wet section of the dehumidifier model to determine the distribution of  $\dot{Q}$ ,  $\dot{m}_{pw}$ ,  $\omega$ ,  $T$ ,  $t_{pw}$ ,  $t_{sw}$  and  $t_I$ . The humidity at the interfacial boundary is obtained as  $\omega_I = \omega_{sat}(p, t_I)$ .

The governing equations for the dry control volume comprise the energy balance on the air side

$$-d\dot{Q} = \dot{m}_{da} dh_a, \quad (21)$$

the heat transfer on the air side

$$d\dot{Q} = h_{ta} (T_\infty - t_0) dA, \quad (22)$$

the energy balance on the seawater side

$$d\dot{Q} = \dot{m}_{sw} c_{psw} dt_{sw} \quad (23)$$

and the heat transfer from the air side of the wall to the seawater to determine the air-side wall surface temperature

$$t_0 = t_{sw} + \frac{dQ}{dA} \left( \frac{d_p}{k_p} + \frac{1}{h_{tsw}} \right). \quad (24)$$

The composition of dry air given by Lemmon et al. [34] is applied to determine the thermophysical properties of dry air. The specific gas constant of dry air  $R_{da} = R_m/M_{da} = 0.287117$  J/(mol K) and the ratio of the molar masses of water and dry air  $M_w/M_{da} = 0.62217 \approx 0.622$  are used for the simulations. The thermophysical properties of humid air are calculated from HuAir [35], those of water from IAPWS-IF97 [36, 37], and those of standard seawater of salinity 35 g/kg from Sharqawy et al. [5].

The governing equations for the dry or wet control volume are solved for each cell successively from the air inlet to the air outlet; starting with an initial guess for the seawater outlet temperature. If the air-side surface temperature is below the air dew point temperature for two successive cells, they form the beginning of the wet section in the heat exchanger. The cells following in air downstream direction are assumed to be wet as well. The system of governing equations for dry or wet control volumes is solved by a trust region dogleg algorithm [38].

## Heat Transfer Correlations

The flow in a dehumidifier with flat parallel plates (Fig. 2) is equivalent to that in a flat duct with heat transfer from both plates for the middle ducts. The two outermost ducts through which humid air flows are assumed adiabatic to the ambient. They are thus calculated both together as a single duct. As  $W \gg D_a$  and  $D_{sw}$ , the known results for heat transfer from parallel plate ducts can be used [39], with the hydraulic diameter  $D_h = 2 D_a$  and  $D_h = 2 D_{sw}$ , respectively. The local heat transfer correlations at position  $z$  for constant wall temperature from Gnielinski [40-43], Table 1, are used with the thermophysical properties at the arithmetic mean fluid temperature between cell inlet and outlet. The critical Reynolds number ranges from 2200 to 3600 [42], depending on the inlet conditions.  $Re_{crit} = 2300$  is selected, following Gnielinski [42]. For the transition region a

linear interpolation between the local Nusselt number for laminar flow at  $Re = 2300$  and the local Nusselt number for turbulent flow at  $Re = 10^4$  is applied [43].

Heat transfer in the condensate film is taken into account according to Nusselt's laminar film condensation theory [30]. As simulations show that the heat transfer resistance of the condensate film is small compared to the air-side heat transfer resistance, a more advanced method for the heat transfer in the condensate film is not required.

## Determination of Pressure Drop

Generally a trade-off between good heat transfer characteristics with a small heat transfer area (low investment costs) against a low energy consumption of fans and pumps (low operating costs) has to be made.

The pressure drop in the single-phase region of a heat exchanger consists of a geodetic pressure drop  $dp_g$ , an inlet and an outlet pressure drop  $dp_M$ , a frictional pressure drop  $dp_f$  and a deceleration pressure gain  $dp_{dec}$ . The total pressure drop in air and seawater flow is

$$\Delta p = \int_0^L \left( \frac{dp_g}{dz} + \frac{dp_f}{dz} + \frac{dp_{dec}}{dz} \right) dz + \Delta p_M. \quad (25)$$

The geodetic pressure drop results from the change of height

$$dp_g = -\rho g dz \quad (26)$$

and can be neglected here.

The inlet and outlet pressure drop

$$\Delta p_M \approx K \frac{\rho w^2}{2} \quad (27)$$

with the loss coefficient  $K$ , which depends on the flow contraction and expansion area ratio and the Reynolds number, is determined with data from Kays [44].

The frictional pressure drop is

$$dp_f = \xi \frac{dz}{D_h} \rho \frac{w^2}{2} \quad (28)$$

where  $\xi$  is the Darcy-Weissbach friction factor. Smooth surfaces are assumed, so the friction factor is independent of the surface roughness [45]. For laminar parallel plate duct flow ( $Re \leq 2300$ )

$$\xi = \frac{64}{2/3Re} = \frac{96}{Re} \quad (29)$$

is applied and for turbulent and transition parallel plate duct flow ( $2300 < Re < 10^6$ )

$$\xi = (1.8 \lg(2/3Re) - 1.5)^{-2} \quad (30)$$

is used.

During the condensation of the water vapor, the fluid flow is decelerated and a pressure gain results

$$dp_{dec} = \left( \frac{\dot{m}}{A_c} \right)^2 \left( \frac{1}{\rho_g} - \frac{1}{\rho_f} \right) d\omega. \quad (31)$$

For condensation on a vertical surface, two-phase flow with separate liquid and gas flow is the most common flow type [46]. For this case, the friction factor in Eq. (28) is determined by the method of Andreussi [47] described in [46].

## Sensitivity Analysis

To show the effect of increasing the number of cells in the simulation model, a sensitivity analysis shown in Fig. 3 is performed for the model with the given configuration. The number of cells in the flow direction used to discretize the heat exchanger is varied from 10 to 150 in increments of ten. The product water temperature change sensitivity is about an order of magnitude larger than the other sensitivities. For an increase from 90 to 100 cells, the relative change is 0.26 % for the product water temperature change and less than 0.05 % for the other quantities. In a sensitivity analysis with a constant seawater-side heat transfer coefficient, the product water temperature is less sensitive than all the other quantities. This shows that the slower decrease in product water temperature change results from discretization of the strongly-varying heat transfer in the seawater and air inlet regions. To reduce this negative effect on the sensitivity, the grid is refined at the seawater and at the air inlet and outlet. For the discretization with 100 cells, the estimated total error is 2.5 % for the product water temperature change and

about 0.13 % for the other quantities. With 100 cells a trade-off between high accuracy and reasonable simulation time is achieved.

## Validation

In a first step, agreement of a simplified numerical model with the solution of an analytical logarithmic mean temperature difference model was demonstrated [9]. In a second step, the results of the simulation are compared to experimental data. We describe this in detail.

From McQuiston's experiments for flat-plate dehumidifiers [48,49] his series 400 without condensation and his series 3000 with condensation from humid air are used to validate the numerical model. Those results are used to validate the presented countercurrent flow model, while McQuiston investigated a cross-flow configuration, because the cooling-water temperature change in the experiments is small making those results usable here.

A comparison of the Nusselt number between experimental data from McQuiston and the heat transfer correlations from Table 1 (VDI Heat Atlas) is presented in Fig. 4. The experimental data from series 400 deviate by as much as 32 % from the VDI Heat Atlas correlations. For the height to width ratio  $D_d/W = 1/24$  of the experimental data, it is reasonable to regard the flat ducts in the heat exchanger as parallel plate ducts. Therefore the correlations from Table 1 are an appropriate representation. It is noticeable that the shape of the experimental data differs from that of the correlations.

Experimental Nusselt numbers for a wet surface in series 3000 in Fig. 4 clearly differ from those for dry surfaces in series 400. By applying the correction factor given by McQuiston [48]

$$h_{ta,wet} = h_{ta,dry} (0.164 \ln Re - 0.02) \quad (32)$$

to the heat transfer correlations, the differing trend is corrected. However, experimental Nusselt numbers in the laminar and lower transition region still differ by as much as 40 % from the correlations of the VDI Heat Atlas.

The humidity ratios at the heat exchanger inlet and outlet are determined from McQuiston's observed wet and dry bulb temperatures for the validation according to Baehr and Stephan [32]. A difference of 1 to 3 g/kg between the inlet and outlet humidity



ratio in McQuiston's dry experiments (series 400) is detected, although both should be identical, as there is no condensation during the dry experiments. McQuiston measured temperatures to an accuracy of 0.14 K [48], which leads to a deviation of less than 0.32 g/kg in the humidity ratio for the experiments in series 400 and does not explain the above-mentioned discrepancy in the experimental humidity ratio.

As the Nusselt number correlations do not match McQuiston's Nusselt number correlations, the experimental results for the heat transfer coefficient are used directly to validate the simulations, since the aim is not to validate Nusselt number correlations, but the numerical model itself. Figure 5 shows a comparison of the series 3000 experiments under wet conditions with the numerical simulation. The results are presented for simulations in which the inlet humidity ratio is determined from McQuiston's experiments. Comparing the numerical and experimental outlet humidity ratios, a deviation of less than 0.4 g/kg or 16.9 % is observed. This difference can be explained partly by the temperature measurement error which leads to an uncertainty of 0.32 g/kg. In the worst case, the heat flow from the experiment is 65 W or 10.3 % lower than that predicted by the simulation. The simulated air temperature reduction is as much as 1.05 °C, or 17.0 % below the experimental value. The measurement error of 0.14 K only partially explains this deviation. The simulated cooling water outlet temperature deviates by up to  $\pm 0.03$  °C, which is less than the accuracy of 0.14 K. The average absolute deviations are 4.6 % for the change of the humidity ratio, 2.4 % for the heat flow, 10.0 % for the change in air temperature and 2.1 % for the change in cooling water temperature.

The error of as much as 3 g/kg observed in McQuiston's dry heat transfer experiments is assumed for the wet experiments too. To assess the effect on the heat exchanger performance, the simulations are performed for different inlet humidities. The simulation results for an inlet humidity deviation of  $\pm 1$  g/kg are shown along with the other results in Fig. 5. A deviation of  $\pm 1$  g/kg in the measured inlet humidity ratio explains the outlet humidity ratio deviation and the cooling water temperature change deviation for all experiments, and the heat flow deviation for all except the fifth experiment which is still 15 W below the range of the simulations. The measurement errors of  $\pm 1$  g/kg and the temperature measurement error of 0.14 K can explain only a small part of the deviation of the air temperature change, which leaves a difference of up to 0.81 K.

Other factors that lead to a deviation between experiment and simulation are: different inlet conditions in the experiment, cross flow in the experiment as opposed to countercurrent flow in the simulation, temperature measurement errors of 0.14 °C, and heat transfer from the fin at the front of the plate (1/3 of total plate length) which could not be taken into account in the simulations.

It is estimated from the dry experiments, by comparing the experimental heat flow to the heat flow for pure countercurrent flow (using the mass flow from the Reynolds number), that the inlet fin used in the experiment accounts for 3 to 7 % of the total heat transfer.

The comparison between the experimental results and the numerical simulations shows that the developed model for flat-plate heat exchangers is accurate within the observed experimental accuracy. It is therefore appropriate to use the model for the simulations and the design of a flat-plate heat exchanger. For the simulations the heat transfer correlations from Table 1 are applied instead of McQuiston's experimental data, as these are most appropriate to the present geometry.

## **SIMULATION OF THE DEHUMIDIFIER**

### **Typical Operating Condition and Heat Exchanger Dimensions**

Simulations are performed for the operating point shown in Fig. 6, a result of an entropy generation minimization for the whole HDH system [50], with the seawater outlet temperature adjusted for seawater operation. The required heat flow of 169 kW is assumed as the criterion to identify suitable heat exchanger geometries.

For simulations, the dimensions of the plate heat exchanger designed by Müller-Holst [12] are used as a reference: Standard PP plates can be as thin as 2 mm, and with a special treatment the plate thickness can be reduced to 0.7 mm. The standard plate spacing on the seawater side is about 3 mm. For PP plates, Müller-Holst [12] recommends an air-side plate spacing of at least 10 mm to prevent direct contact between the plates resulting from plate expansion. Whether changes in design or material permit a lower minimum PP plate spacing has to be checked. If metal plates are used instead, the spacing can be as low as 4 mm on the air side. Here, magnetite-filled PP plates of a

thermal conductivity  $k_p = 1.0 \text{ W/(m K)}$  [19], thickness  $d_p = 0.7 \text{ mm}$  and seawater-side plate spacing  $D_{sw} = 3 \text{ mm}$  are used unless otherwise stated.

## Plate Length Variation

Figure 7 shows results for different heat exchanger lengths  $L$  from 0.60 m to 2.20 m in the flow direction, with a plate width of 12.11 m, an air-side plate spacing of 10 mm and inlet conditions as in Fig. 6. To obtain feasible geometries, the plate width is subdivided into several parallel plates. The air-side inlet velocity is 6.7 m/s and the seawater-side inlet velocity is 0.036 m/s. In all figures with the flow length as abscissa, the air flows from left to right, with countercurrent seawater flow from right to left.

The air bulk, the interfacial boundary, the air-side plate surface and the seawater bulk temperature for five different heat exchanger lengths are shown in Fig. 7 (top). For all geometries, the seawater temperature increases in the flow direction (from right to left) at a slightly increasing gradient. The temperature of the countercurrent air flow decreases, with a declining slope. Towards the end of the plates, the developing seawater flow and reduced latent heat transfer result in this more pronounced air temperature reduction. The product water temperature follows the seawater temperature trend, as the heat transfer resistance between seawater and interfacial boundary varies little along the flow length, in contrast to the air-side heat transfer resistance. Owing to the improved heat transfer at the air inlet and at the seawater inlet, the product water temperature is closer to the air temperature at the air inlet and closer to the seawater temperature at the seawater inlet. Differences between the interfacial boundary and the air-side plate surface temperatures are small; therefore, a more detailed model of the condensate film is not required and it is not necessary to distinguish between film and dropwise condensation. In common air-conditioning dehumidifiers the heat transfer resistance of the condensate film is negligible, whereas in condensation without non-condensibles the condensate film imposes the main heat transfer resistance. HDH dehumidifiers operate somewhere between these two extremes. The heat transfer resistance of the condensate film ( $3 \text{ to } 16 \times 10^{-5} \text{ m}^2\text{K/W}$ ) can be neglected in future models to reduce the simulation time.

Figure 7 (center) shows the bulk flow humidity ratio and the interfacial boundary humidity ratio distribution. The bulk flow humidity ratio decreases almost linearly. The

form of the humidity ratio at the interfacial boundary is determined by the temperature at the interfacial boundary. At first the decrease is pronounced due to the increased air inlet heat transfer. Towards the end of the heat exchanger the decrease is less pronounced, and the difference between bulk and interface humidity ratio becomes smaller. The common assumption of saturated air at the dehumidifier outlet [3] is confirmed for sufficiently large heat transfer area. As soon as the air bulk flow reaches saturation, a very small amount of mist is generated. However, this is negligible relative to the mass flow of product water, so no mist eliminator is required at the dehumidifier outlet. As the outlet air is saturated, measures are needed to prevent corrosion due to condensation in the ducts leaving the dehumidifier, e.g. a heater directly after the dehumidifier outlet, or appropriate insulation of the ducts to prevent condensate formation on cold surfaces.

Figure 7 (bottom) presents the product water mass flow for the various heat exchanger lengths. Extending the heat exchanger length from 0.60 m to 1.00 m, 1.40 m, 1.80 m or 2.20 m increases the condensate production by 34 %, 58 %, 75 % or 96 %, respectively. The heat exchanger length selected depends upon the economic value of the additional product water. At the air inlet the product water production is especially high. In the fully-developed flow region the mass transfer driving force, and thus the local product water production decrease.

Because of the condensation of water vapor and the air temperature reduction, the air flow velocity and Reynolds number decline considerably in the flow direction by about 30 %. The air-side heat transfer coefficient falls rapidly in the inlet region to an almost constant value of about  $12.5 \text{ W}/(\text{m}^2\text{K})$  in the fully-developed flow region, which begins at less than 0.25 m flow length.

## **Geometries Determined for the Operating Point**

A large number of simulations were performed for the operating point shown in Figure 6 to determine suitable heat exchanger geometries [9]. Three different air-side plate spacings  $D_a = 7 \text{ mm}$ ,  $10 \text{ mm}$  and  $20 \text{ mm}$  are examined for various plate lengths and widths. Some of those which lead to the inlet conditions and the heat flow of the operating point indicated in Fig. 6 are presented here.

Results for an air-side plate spacing of 10 mm are shown in Figs. 8 to 10 for combinations of plate length and width as in Table 2. At constant volumetric air flow rate, the air flow velocity decreases with increasing plate width  $W$ . The air inlet velocity ranges from 2.8 m/s to 10.0 m/s; some resulting mean velocities are given in Table 2.

Figure 8 displays the temperature distributions in air bulk, product water and seawater for various heat exchanger lengths and widths; these are similar to the temperature distributions shown in Fig. 7. The product water and air outlet temperatures are marginally influenced by the plate dimensions that yield the same heat flow. As the plate length increases, the product water outlet temperature increases slightly too, from 19.9 °C to 21.9 °C for the simulations shown. The lower flow velocity for short, wide plates results in a longer product water residence time. According to the energy balance on the air side, the air outlet temperature varies from 42.2 °C to 42.3 °C, which is 1.2 K to 1.3 K above the operating point air outlet temperature of Fig. 6.

Figure 9 shows the bulk flow and the interfacial boundary humidity ratio distribution. The humidity ratio of the bulk flow decreases almost linearly to 0.132 kg/kg so that a product water mass flow of  $\dot{m}_{pw} = 0.0644$  kg/s results. The resultant ratio of heat transfer area to product water mass flow given in Table 2 ranges from 296.0 m<sup>2</sup>/(kg/s) to 412.5 m<sup>2</sup>/(kg/s) and depends on the operating point and geometry. The outlet humidity ratio is higher than that for the operating point because of the higher air outlet temperature. The pressure drop is lower than in Fig. 6 which has a smaller influence on the saturated humidity ratio than the increased temperature.

Because of the condensation of water vapor and the air temperature reduction, the air flow velocity decreases in flow direction, cf. Fig. 10. The air-side heat transfer coefficient decreases in the inlet region to an almost constant value of 10.3 W/(m<sup>2</sup>K) in the fully-developed laminar flow region. For transition flow ( $2300 \leq Re \leq 10^4$ ), the heat transfer coefficient is higher than that for laminar flow.

The same trends described for an air-side plate spacing of 10 mm are apparent for a 20 mm and a 7 mm spacing, too.

For 20 mm plate spacing the plate width range is selected to achieve an air inlet velocity in the range from 2.9 m/s to 10 m/s. To obtain the required heat flow, combinations of plate length from 3.05 m to 5.00 m and width from 4.06 m to 14.06 m

are investigated. For each plate length, one particular width results in the required heat flow; some of these combinations are shown in Table 3. With increasing air flow velocity the heat transfer area decreases because the mean air-side heat transfer coefficient increases. For fully-developed flow the air-side heat transfer coefficient is 6.2 W/(m<sup>2</sup>K) to 11.6 W/(m<sup>2</sup>K). The air outlet temperature ranges from 42.2 °C to 42.5 °C, and the seawater outlet temperature is 46.5 °C. With an outlet humidity ratio of about 0.132 kg/kg, a product water mass flow of about 0.0644 kg/s results. The ratio of heat transfer area to product water mass flow ranges from 313.8 m<sup>2</sup>/(kg/s) to 669.3 m<sup>2</sup>/(kg/s).

Simulations for an air-side plate spacing of 7 mm were performed to show the improvement possible when the lower limit of the plate spacing is below 10 mm. To achieve the required heat flow for a spacing of 7 mm, combinations of plate length from 0.50 m to 1.58 m and width from 11.59 m to 41.59 m are considered, with air inlet velocities from 2.8 m/s to 10 m/s. Some of these are listed in Table 3. All combinations within the laminar flow regime have a similar heat transfer area, as the mean air-side heat transfer coefficient for the rapidly fully-developed flow varies little. For fully-developed air flow the air-side heat transfer coefficient is 14.4 W/(m<sup>2</sup>K). The air outlet temperature is 42.2 °C, the seawater outlet temperature 46.5 °C. The outlet humidity ratio of 0.132 kg/kg results in a product water mass flow of 0.0644 kg/s, approximately the same as for the simulations with plate spacing 10 mm and 20 mm. The ratio of heat transfer area to product water mass flow ranges from 238.2 m<sup>2</sup>/(kg/s) to 322.3 m<sup>2</sup>/(kg/s).

Figure 11 shows the air-side pressure drop as a function of the plate length and the plate width for the inlet conditions and heat flow from Fig. 6 with air-side plate spacings of 7 mm, 10 mm and 20 mm. The pressure-drop dependence on plate length and plate width is also shown, as projections of the curves. Contours of constant heat transfer area are indicated by curves in the (length, width) plane. At low flow velocity the air flow is laminar for  $D_a = 7$  mm and 10 mm; the required heat transfer area is nearly independent of the air flow velocity, as the air-side heat transfer coefficient is independent of the air flow velocity in the developed flow range. In the laminar range the pressure drop is comparatively low. It slowly increases with increasing air velocity. As the pressure drop in the laminar region increases whilst the heat transfer area remains constant, plates which result in an air flow just below the transition to turbulent flow are unfavorable. At

the onset of this transition, the air-side heat transfer coefficient in the developed flow region increases with air flow velocity, which reduces the required heat transfer area but considerably increases the pressure drop. So plates should be either short and wide (laminar flow) or long and narrow (transition or turbulent flow) to achieve low operating costs or low investment costs, respectively.

For a given flow velocity, a greater air-side plate spacing always results in a lower pressure drop, but a larger heat transfer area is required to achieve the same heat flow, and the increased plate spacing results in a bulkier dehumidifier. For a given heat flow and heat transfer area, but variable plate length and width, a greater plate spacing results in a higher pressure drop. To keep the required heat transfer area and the pressure drop low, the air-side spacing should be as small as possible. A 10 mm plate spacing is recommended, as this is known to be practicable [12]. The extent to which the minimum air-side spacing of the proposed magnetite-filled PP plates could be reduced below this known limit remains to be tested.

## **Variation of Plate Conductive Heat Transfer Resistance**

The plate's thickness and thermal conductivity determine its conductive heat transfer resistance. The influence of both factors on the performance of a heat exchanger with plate length  $L = 1.93$  m, plate width  $W = 12.11$  m, air-side plate spacing  $D_a = 10$  mm and inlet conditions from Figure 6 is shown in Figure 12. The plate thickness scale (top) applies to magnetite-filled PP plates of moderate thermal conductivity  $k_p = 1.0$  W/(m K). For pure PP, a minimum plate thickness of 0.7 mm is known to achieve mechanical stability [12]. This limit will be lower for magnetite-filled PP plates, which have better mechanical properties [20].

The case of 0 mm plate thickness, i.e. without heat transfer resistance of the plate, is used as a reference to assess the effect of the conductive heat transfer resistance of the magnetite-filled PP material. The resistance of the 0.7 mm thick plate (dashed line) reduces the heat flow and condensate production by 4.2 % relative to the reference case. A plate of thickness of e.g. 2 mm (top scale) that allows a higher pressure difference between air and seawater sides reduces the heat flow and condensate production by 11.3

% . The heat transfer resistance of a 0.07 mm thick plate (top scale) reduces the heat flow by 2.4 % . In general the plate thickness should be kept as low as possible.

The thermal conductivity scale (bottom) applies to a plate thickness of 0.7 mm. If titanium alloy plates of this thickness and a thermal conductivity of  $k_p = 21.9 \text{ W/(m K)}$  are used, the thermal performance is almost the same as in the absence of thermal conductive plate resistance.

Pure PP plates of thermal conductivity  $0.22 \text{ W/(m K)}$  reduce the heat flow by 17.3 % relative to titanium alloy plates. The maximum reported conductivity of PP with embedded Cu particles is  $2.5 \text{ W/(m K)}$ , which results in a heat flow only 3.9 % lower than that for titanium alloy plates. Comparing the small improvement of embedded copper particles over magnetite particles to the threat of corrosion, copper particles are not recommended.

As space scarcely imposes a critical constraint upon HDH desalination systems, the slightly greater heat transfer area required by filled PP plates is acceptable, whereas the high price of a titanium alloy heat exchanger would considerably increase the total investment cost for an HDH desalination system.

The addition of particles to reduce the thermal conductive resistance of the PP plates improves heat exchanger performance. The heat flow reduction is small relative to the heat flow achievable with more expensive titanium alloy plates and the seawater corrosion resistance high, so the use of particle embedded PP materials helps reduce the cost relative to titanium alloy plate heat exchangers, and increases the thermal performance relative to pure PP heat exchangers. The difference in performance between titanium alloy and PP plates increases further if air-side heat transfer is improved. Particle embedded PP plates are therefore especially useful for heat exchangers with laminar air flow.

### **Influence of Seawater-Side Plate Spacing**

Although heat and mass transfer on the air side dominate the performance of the dehumidifier, the influence of the seawater-side heat transfer is investigated, too. For the given mass flow ratio of Fig. 6, the seawater flow velocity is much smaller than the air flow velocity for pure countercurrent flow with similar air-side and seawater-side plate



spacings. Because of the geometrical constraints (minimum seawater-side plate spacing and maximum heat exchanger length), the flow velocities in the flat-plate heat exchanger cannot be increased sufficiently for the mass flow ratios in HDH systems to prevent particles settling for pure countercurrent flow. Therefore, seawater pretreatment is important.

The effect of seawater-side plate spacing on heat exchanger performance is shown in Fig. 13. The indicated standard seawater-side plate spacing of 3 mm results in a heat flow about 7.1 % lower than that for ideal heat transfer on the seawater side.

As the heat exchanger performance varies with the seawater-side plate spacing, convective heat transfer on the seawater side cannot be neglected. The mechanical power required to circulate the seawater mass flow is small relative to that for the air mass flow. Increasing the seawater flow velocity to achieve a higher seawater heat transfer coefficient is thus of advantage, even though the seawater pressure drop increases too. To avoid a large seawater-side heat transfer resistance and reduce fouling due to low flow velocity even at 3 mm plate spacing, the seawater can be conducted in meander channels inserted into the plates in the cross-flow direction to increase the seawater velocity, as indicated in Fig. 13. For the geometry simulated, the use of six baffles in a heat exchanger with twelve 1.01 m wide plates to create seven cross channels leads to an estimated heat flow reduction of only 2.1% relative to perfect seawater-side heat transfer. A meander flow configuration on the seawater side improves the thermal performance. It increases the seawater flow velocity as well, which may reduce fouling.

### **Influence of Fouling on Heat Exchanger Performance**

A comparison of simulations with the fouling resistance of  $R_f = 0.043 \text{ m}^2\text{K/kW}$  and without it reveals an influence on the heat flow in the order of 1 % for PP plates, stainless steel plates and titanium alloy plates. Although seawater fouling is an important aspect for the smooth operation of the dehumidifier, it has a minor influence on its thermal performance, as the air-side heat transfer resistance dominates.

### **Effect of Varying Plate Length and Width**

To investigate the influence of the plate size, many simulations were performed for the inlet conditions of the operating point. Figures 14 and 15 show the air outlet temperature and the heat flow as functions of heat transfer area and air-side pressure drop for different plate length/width combinations with an air-side plate spacing of 10 mm. The black mesh indicates constant length between 0.30 m and 2.20 m and constant width between 8.11 m and 29.11 m in increments of 0.10 m and 1.00 m, respectively. In both figures, the lines of positive slope in the (heat transfer area, air-side pressure drop) plane indicate constant width and increasing length. The additional length adds to the frictional pressure drop, so the total pressure drop grows linearly. The air-side pressure drop is a function of squared flow velocity, which decreases with increasing the plate width. Lines of negative slope represent constant length and increasing width.

The white dashed line which indicates the mean Reynolds number  $Re_a = 2300$  divides the figure into a lower laminar and an upper transition air flow region. Since the quantity of condensed vapor varies, the line does not represent a constant width. Slightly below this line, the first section in the heat exchanger is already in the transition region and slightly above this line, the final section of the heat exchanger is still laminar. For laminar flow, outlet conditions are constant for a given heat transfer area. In the transition region, heat transfer depends upon flow velocity, and outlet conditions depend upon plate length and width. Simulations corresponding to the heat flow of Fig. 6 are indicated by the gray line. Again, the required heat transfer area is seen to be constant in the laminar region and starts to decrease in the transition region.

Figure 14 illustrates the dependence of air outlet temperature on the air-side pressure drop and heat transfer area. For small heat transfer area and air-side pressure drop the air outlet temperature is high; for large heat transfer area it is low. At constant heat transfer area, the air outlet temperature slightly decreases with increasing pressure drop in the transition region.

The most important measures of dehumidifier performance are: the heat flow, the air-side pressure drop as a measure of operating costs, and the heat transfer area as a measure of equipment costs. Their relationship is shown in Fig. 15. In the laminar air flow region, the heat flow increases with the heat transfer area but is independent of the air flow velocity. Laminar air flow results in the lowest heat flow for a given heat transfer area.

The slope of the minimum laminar heat flow decreases with increasing heat transfer area, as the mass transfer driving force is reduced. In the transition region, the heat flow and the air-side pressure drop increase with increasing air flow velocity. The additional air-side pressure drop expected for a particular heat transfer area reduction is apparent. The quantity of condensate per heat flow is constant for a given total heat flow, but decreases with increasing heat flow.

## Conclusions

Flat-plate heat exchangers are evaluated for use as dehumidifiers in HDH desalination systems. A typical HDH dehumidifier operating point which results in minimum entropy production for the overall system is chosen. The operating range exceeds the validity range of common air-conditioning models, so a new model is developed, including the use of a logarithmic mass transfer driving force. Mass transfer coefficients are determined according to the Chilton-Colburn heat and mass transfer analogy together with an accurate Lewis number. The Ackermann correction allows for the effect of condensation on sensible heat transfer, leading to an increase of the sensible heat transfer coefficient of up to 30 %. The model is applicable to fully dry, fully wet, and partially wet operation. Inlet and outlet pressure drop due to abrupt contraction and expansion [44], the frictional pressure drop for single-phase [45] and two-phase flow [47], and the deceleration pressure gain due to the condensation of water vapor, are taken into account. The heat exchanger is discretized into many cells and modeled by the cell method [22]. The model is validated with the aid of experimental results for flat-plate dehumidifiers from McQuiston [48]. Major conclusions of this study are as follow.

1. Despite the increased condensate production rate relative to air-conditioning systems, simulations for film condensation show that the effect of heat transfer through the condensate film is negligible relative to other heat transfer resistances for flat-plate heat exchangers.
2. Simulations with the flat-plate heat exchanger model for polypropylene (PP), stainless steel and titanium alloy plates show that seawater fouling has little effect upon thermal performance.

3. The low thermal conductivity of PP leads to a 17.3% lower heat flow for pure PP plates relative to titanium alloy plates with the same heat exchanger geometry. To minimize this disadvantage, particle embedded PP plates are proposed. Relative to titanium alloy plates, the heat flow is reduced by only 3.9% to 17.3%, depending upon the plate thermal conductivity achieved. The increase in required surface area is acceptable in view of the considerably reduced equipment cost.
4. If the air and seawater sides operate at the same pressure, the plate thickness can be as low as 0.7 mm. If the pressure difference between the fluids is large, the minimum plate thickness must be greater, which has a pronounced effect upon the thermal performance of the heat exchanger. A polymer heat exchanger thus offers no advantage for certain applications with high pressure differences.
5. Simulations show that the thermal performance is sensitive to the seawater-side plate spacing and that seawater-side plate spacings below 3 mm are desirable because of the increased seawater flow velocity. A minimum spacing limit is imposed by the production technology and by the accumulation of a fouling film, so the use of baffles or channels on the plate surface to increase the flow velocity is investigated.
6. For given heat flow and heat transfer area, the air-side pressure drop decreases with decreasing air-side plate spacing. The heat exchanger compactness on the other hand decreases considerably for larger air-side plate spacing. The lowest possible air-side plate spacing is therefore recommended.
7. Short, wide plates yield low pressure drop and long, narrow plates yield low surface area. The plate size chosen represents a compromise between pressure drop and heat transfer area.

## **Acknowledgments**

The authors would like to thank the German Academic Exchange Service (DAAD), the K. H. Ditze foundation and the E. Meurer foundation for supporting M. Sievers' stay

at the Massachusetts Institute of Technology. J.H. Lienhard V acknowledges support from King Fahd University of Petroleum and Minerals through the Center for Clean Water and Clean Energy at MIT and KFUPM.

## Nomenclature

$A$	area, $\text{m}^2$
$A_c$	cross-sectional area, $\text{m}^2$
$c$	molar concentration, $\text{mol m}^{-3}$
$c_p$	specific heat capacity at constant pressure, $\text{J kg}^{-1} \text{K}^{-1}$
$D$	diffusion coefficient, $\text{m}^2 \text{s}^{-1}$
$D_a$	air-side plate spacing, m
$D_{sw}$	seawater-side plate spacing, m
$D_h$	hydraulic diameter, m
$d_p$	plate thickness, m
$g$	acceleration due to gravity $g = 9.80665 \text{ m s}^{-2}$
$H$	heat exchanger height, m
$h$	specific enthalpy, $\text{J kg}^{-1}$
$h_{fg}$	specific latent heat of vaporization, $\text{J kg}^{-1}$
$h_m$	mass transfer coefficient, $\text{m s}^{-1}$
$h_t$	heat transfer coefficient, $\text{W m}^{-2} \text{K}^{-1}$
$h_{ta}^*$	heat transfer coefficient on air side with Ackermann correction, $\text{W m}^{-2} \text{K}^{-1}$
$K$	total (pressure) loss coefficient
$k$	thermal conductivity, $\text{W m}^{-1} \text{K}^{-1}$
$L$	plate length, m
$Le$	Lewis number, $Le = \alpha D^{-1}$
$M$	molar mass, $\text{g mol}^{-1}$
$m$	Prandtl number exponent
$\dot{m}$	mass flow rate, $\text{kg s}^{-1}$
$Nu$	Nusselt number, $Nu = h_t D_h^{-1} k^{-1}$
$p$	pressure, Pa
$Pr$	Prandtl number, $Pr = \mu \rho^{-1} \alpha^{-1}$
$\dot{Q}$	heat flow, W
$Re$	Reynolds number, $Re = w D_h \rho \mu^{-1}$
$R_f$	fouling resistance, $\text{m}^2 \text{K W}^{-1}$
$S$	salinity of seawater, $\text{kg kg}^{-1}$
$Sc$	Schmidt number, $Sc = \mu \rho^{-1} D^{-1}$
$Sh$	Sherwood number, $Sh = h_m D_h D^{-1}$
$T$	air temperature in bulk flow, K
$t_{sw}$	seawater temperature in bulk flow, K
$t_{pw}$	product water temperature, condensate temperature, K
$W$	plate width, m
$w$	flow velocity, $\text{m s}^{-1}$
$x_i$	mole fraction of species i, $\text{mol mol}^{-1}$
$y$	coordinate, m
$z$	coordinate, m

### **Greek Symbols**

$\alpha$	thermal diffusivity, $\text{m}^2 \text{s}^{-1}$
$\delta$	thickness of condensate film, m
$\zeta$	Ackermann correction
$\mu$	dynamic viscosity, $\text{kg m}^{-1} \text{s}^{-1}$
$\xi$	Darcy-Weissbach friction factor
$\rho$	mass density, $\text{kg m}^{-3}$
$\phi$	relative humidity
$\omega$	humidity ratio, $\text{kg kg}^{-1}$

### **Subscripts**

0	wall surface on condensate side
$\infty$	in air bulk flow
<i>a</i>	humid air
<i>da</i>	dry air
<i>dec</i>	deceleration
<i>dry</i>	dry surface
<i>f</i>	liquid
<i>f</i>	friction
<i>g</i>	vapor, gaseous
<i>I</i>	at the interfacial boundary between air and condensate
<i>l</i>	laminar
<i>p</i>	plate
<i>pw</i>	product water
<i>t</i>	turbulent
<i>sat</i>	at saturation
<i>sw</i>	seawater
<i>sww</i>	wall surface on seawater side
<i>w</i>	water
<i>wet</i>	wet surface
<i>wg</i>	water vapor
<i>z</i>	in z direction

## References

- [1] Stephan, K., *Die Gewinnung von Trink- und Brauchwasser. Eine der wichtigsten Aufgaben zur Überwindung der Nahrungs- und Energiekrise*, Snage i Putovi Rata i Mira, Yugoslavian Academy of Science, pp. 703-723, Zagreb, 1978.
- [2] Narayan, G.P., Sharqawy, M.H., Lienhard V, J.H., and Zubair, S.M., *Thermodynamic analysis of humidification dehumidification desalination cycles*, Desalination and Water Treatment, vol. 16, no. 1-3, pp. 339-353, 2009.
- [3] Narayan, G.P., Sharqawy, M.H., Summers, E.K, Lienhard V, J.H., Zubair, S.M., and Antar, M.A., *The potential of solar-driven humidification-dehumidification desalination for small scale decentralized water production*, Renewable and Sustainable Energy Reviews, vol. 14, no. 4, pp. 1187-1201, 2010.
- [4] Mistry, K.H., Lienhard V, J.H., and Zubair, S.M., *Effect of entropy generation on the performance of humidification-dehumidification desalination cycles*, International Journal of Thermal Sciences, vol. 49, no. 9, pp. 1837-1847, 2010.
- [5] Sharqawy, M.H., Lienhard V, J.H., and Zubair, S.M., *Thermophysical properties of seawater: A review of existing correlations and data*, Desalination and Water Treatment, vol. 16, no. 1-3, pp. 354-380, 2010.
- [6] Summers, E.K., Lienhard V, J.H., and Zubair, S.M., *Air-heating solar collectors for humidification-dehumidification desalination systems*, Journal of Solar Energy Engineering, vol. 133, no. 1, 011016, 2011.
- [7] Sharqawy, M.H., Lienhard V, J.H., and Zubair, S.M., *On thermal performance of seawater cooling towers*, Journal of Engineering for Gas Turbines and Power, vol. 133, no. 4, pp. 43001-43007, 2011.
- [8] Narayan, G.P., Zubair, S.M., and Lienhard V, J.H., *Status of humidification-dehumidification desalination*, IDA Journal, in press, 2012.
- [9] Sievers, M., *Design and optimization of a dehumidifier in a humidification-dehumidification (HDH) desalination system*, Diploma thesis. Hamburg University of Technology, Germany, 2010.



- [10] Lotz, H., *Plattenwärmetauscher*, in *Handbuch der Kältetechnik*, eds. Steimle, F., Stephan, K., vol. 6B, Springer, Berlin., 1988.
- [11] Ayub, Z.H., *Plate heat exchanger literature survey and new heat transfer and pressure drop correlations for refrigerant evaporators*, *Heat Transfer Engineering*, vol. 24, no. 5, pp. 3-16, 2003.
- [12] Müller-Holst, H., *Mehrfacheffekt-Feuchtluftdestillation bei Umgebungsdruck – Verfahrensoptimierung und Anwendungen*, Dissertation, Technische Universität München, Germany, 2002.
- [13] Müller-Holst, H., *Solar Thermal Desalination Using the Multiple Effect Humidification (MEH)-Method*, in *Solar Desalination for the 21st Century*, eds. Rizzuti, L. et al., Springer Netherlands, pp. 215-225, 2007.
- [14] GEA PHE Systems, *GEA PHE Systems liefert Plattenwärmetauscher für wegweisende Meerwasserentsalzungsanlage*, 2010, [http://www.gea-phe.com/germany/themes/news-info/aktuelle-meldungen/aktuelle-meldungen/?tx\\_ttnews%5Btt\\_news%5D=298&cHash=ac09332bd7](http://www.gea-phe.com/germany/themes/news-info/aktuelle-meldungen/aktuelle-meldungen/?tx_ttnews%5Btt_news%5D=298&cHash=ac09332bd7), accessed 07/21/2010.
- [15] Franz, M., Private communication, SGL Group, Meitingen, Germany, June 2010
- [16] Neubronner, M., *Stoffwerte von Kunststoffen*, in *VDI-Wärmeatlas* (VDI Heat Atlas), Editor Verein Deutscher Ingenieure (The Association of German Engineers), VDI-Gesellschaft Verfahrenstechnik und Chemieingenieurwesen (GVC), 10th (German) edition, Springer-Verlag, Berlin - Heidelberg - New York, chapter Def, 2006.
- [17] Neubronner, M., Bodmer, T., *Stoffwerte von reinen Metallen und Metalllegierungen*, in *VDI-Wärmeatlas* (VDI Heat Atlas), Editor Verein Deutscher Ingenieure (The Association of German Engineers), VDI-Gesellschaft Verfahrenstechnik und Chemieingenieurwesen (GVC), 10th (German) edition, Springer-Verlag, Berlin - Heidelberg - New York, chapter Dea, 2006.
- [18] Weidenfeller, B., Höfer, M., and Schilling, F. R., *Thermal conductivity, thermal diffusivity, and specific heat capacity of particle filled polypropylene*, *Composites Part A: Applied Science and Manufacturing*, vol. 35, no. 4, pp. 423-429, 2004.

- [19] Weidenfeller, B., Private communication, Technische Universität Clausthal, Institut für Mechanische Verfahrenstechnik, Clausthal, Germany, August 2010.
- [20] Weidenfeller, B., Riehemann, W., and Lei, Q., *Mechanical spectroscopy of polymermagnetite composites*, Material Science and Engineering A, vol. 370, no. 1-2, pp. 278-283, 2002.
- [21] Müller-Steinhagen, H., *Verschmutzung von Wärmeübertragerflächen*, in *VDI-Wärmeatlas* (VDI Heat Atlas), Editor Verein Deutscher Ingenieure (The Association of German Engineers), VDI-Gesellschaft Verfahrenstechnik und Chemieingenieurwesen (GVC), 10th (German) edition, Springer-Verlag, Berlin - Heidelberg - New York, chapter Od, 2006.
- [22] Roetzel, W., Spang, B., *Berechnung von Wärmeübertragern*, in *VDI-Wärmeatlas* (VDI Heat Atlas), Editor Verein Deutscher Ingenieure (The Association of German Engineers), VDI-Gesellschaft Verfahrenstechnik und Chemieingenieurwesen (GVC), 10th (German) edition, Springer-Verlag, Berlin - Heidelberg - New York, chapter Ca, 2006.
- [23] Air-Conditioning, Heating and Refrigeration Institute, AHRI Standard 410-2001 with addendum 2, *Forced-circulation air-heating and air-cooling coils*, Arlington, VA, USA, 2005.
- [24] ASHRAE Handbook, *Heating, Ventilating, and Air-Conditioning Systems and Equipment*, American Society of Heating, Refrigerating and Air-Conditioning Engineers, Inc., Atlanta, GA, 2008.
- [25] Zeller, M., *Be- und Entfeuchten von Luft*, in *VDI-Wärmeatlas* (VDI Heat Atlas), Editor Verein Deutscher Ingenieure (The Association of German Engineers), VDI-Gesellschaft Verfahrenstechnik und Chemieingenieurwesen (GVC), 10th (German) edition, Springer-Verlag, Berlin - Heidelberg - New York, chapter Mk, 2006.
- [26] Sparrow, E.M., Minkowycz, W.J., and Saddy, M., *Forced convection condensation in the presence of noncondensables and interfacial resistance*, International Journal of Heat and Mass Transfer, vol. 10, no. 12, pp. 1829-1845, 1967.

- [27] Stephan, K., and Laesecke, A., *The Influence of Suction on Heat and Mass Transfer in Condensation of Mixed Vapors*, Heat and Mass Transfer, vol. 13, no 1-2, pp. 115-123, 1980.
- [28] Eckels, P.W., and Rabas, T.J., *Dehumidification: On the correlation of wet and dry transport processes in plate finned-tube heat exchangers*, Journal of Heat Transfer vol. 109, no. 3, pp. 575-582, 1987.
- [29] Ackermann, G., *Wärmeübergang und molekulare Stoffübertragung im gleichen Feld bei großen Temperatur- und Partialdruckdifferenzen*, VDI-Forschungsheft, vol. 382, VDI-Verlag, Berlin, pp. 1-16, 1937.
- [30] Lienhard IV, J.H., and Lienhard V, J.H., *A Heat Transfer Textbook*, 4th ed., Dover Publications, Mineola NY, 2011.
- [31] Poppe, M., *Berechnung von Rückkühlwerken*, in *VDI-Wärmeatlas* (VDI Heat Atlas), Editor Verein Deutscher Ingenieure (The Association of German Engineers), VDI-Gesellschaft Verfahrenstechnik und Chemieingenieurwesen (GVC), 10th (German) edition, Springer-Verlag, Berlin - Heidelberg - New York, chapter Mj, 2006.
- [32] Baehr, H. D., and Stephan, K., *Heat and Mass Transfer*, 2nd edition, Springer-Verlag, Berlin - Heidelberg - New York, 2006.
- [33] Sadasivan, P., and Lienhard IV, J.H., *Sensible Heat Correction in Laminar Film Boiling and Condensation*, Journal of Heat Transfer, vol. 109, no. 2, pp. 545-547, 1987.
- [34] Lemmon, E.W., Jacobsen, R.,T., Penoncello, S.,G., and Friend, D.,G., *Thermodynamic Properties of Air and Mixtures of Nitrogen, Argon and Oxygen from 60 to 2000 K at Pressures to 2000 MPa*, Journal of Physical Chemistry Reference Data, vol. 29, no. 2, pp. 331-385, 2000.
- [35] Kretzschmar, H.-J., Stöcker, I., Jähne, I., Herrmann, S., and Salomo, B., *Stoffwertberechnung für feuchte Luft als ideales Gemisch realer Fluide FluidLAB LibHuAir für Matlab*. Hochschule Zittau/Görlitz (FH) - University of Applied Sciences, Fachbereich Maschinenwesen, Fachgebiet Technische Thermodynamik, 2008.

- [36] Wagner, W., and Kretzschmar, H.-J., *International steam tables. Properties of water and steam based on the industrial formulation IAPWS-IF97*, 2nd edition. Springer-Verlag, Berlin, 2008.
- [37] Lemmon, E.W., Huber, M.L., and McLinden, M.O., *NIST Standard Reference Database 23: Reference Fluid Thermodynamic and Transport Properties-REFPROP*, Version 8.0. National Institute of Standards and Technology, Standard Reference Data Program, Gaithersburg, 2010.
- [38] Powell, M.J.D., *A Fortran subroutine for solving systems of nonlinear algebraic equations*, in *Numerical Methods for Nonlinear Algebraic Equations*, Editor Rabinowitz, P., chapter 7, 1970.
- [39] Shah, R.K., and Bhatti, M.S., *Laminar convective heat transfer in ducts*, in Kakac, S., Shah, R.K., and Aung, W., *Handbook of single-phase convective heat transfer*. Wiley & Sons, Hoboken, 1987.
- [40] Gnielinski, V., *Wärmeübertragung im konzentrischen Ringspalt und im ebenen Spalt*, in *VDI Wärmeatlas (VDI Heat Atlas)*, Editor Verein Deutscher Ingenieure (The Association of German Engineers), VDI-Gesellschaft Verfahrenstechnik und Chemieingenieurwesen (GVC), 10th (German) edition, Springer-Verlag, Berlin - Heidelberg - New York, chapter Gb, 2006.
- [41] Gnielinski, V., *Heat transfer coefficients for turbulent flow in concentric annular ducts*, *Heat Transfer Engineering*, vol. 30, no. 6, pp. 431-436, 2009.
- [42] Gnielinski, V., *Heat transfer in concentric annular and parallel plate ducts*, in *VDI Heat Atlas*, Editor Verein Deutscher Ingenieure (The Association of German Engineers), VDI-Gesellschaft Verfahrenstechnik und Chemieingenieurwesen (GVC), 2nd edition, Springer-Verlag, Berlin - Heidelberg - New York, chapter G2, 2010.
- [43] Gnielinski, V., *Ein neues Berechnungsverfahren für die Wärmeübertragung im Übergangsbereich zwischen laminarer und turbulenter Rohrströmung*, *Forschung im Ingenieurwesen*, vol. 61, no. 9, pp. 240-248, 1995.
- [44] Kays, W.M., *Loss coefficients for abrupt changes in flow cross section with low Reynolds number flow in single and multiple tube systems*, Technical Report 9,

- Department of Mechanical Engineering, Stanford University, Transaction of the American Society of Mechanical Engineers, vol. 72, pp. 1067-1074, 1950.
- [45] Gnielinski, V., *Berechnung des Druckverlustes in glatten konzentrischen Ringspalten bei ausgebildeter laminarer und turbulenter isothermer Strömung*, Chemie-Ingenieur-Technik, vol. 79, no 1-2, pp. 91-95, 2007.
- [46] Müller, J., and Numrich, R., *Filmkondensation reiner Dämpfe*, in *VDI-Wärmeatlas* (VDI Heat Atlas), Editor Verein Deutscher Ingenieure (The Association of German Engineers), VDI-Gesellschaft Verfahrenstechnik und Chemieingenieurwesen (GVC), 10th (German) edition, Springer-Verlag, Berlin - Heidelberg - New York, chapter Ja, 2006.
- [47] Andreussi, P., *The onset of drop entrainment in annular downward flows*, Canadian Journal of Chemical Engineering, vol. 58, no. 2, pp. 267-270, 1980.
- [48] McQuiston, F.C., *Heat, mass and momentum transfer in a parallel plate dehumidifying exchanger*, ASHRAE Transactions, vol. 82, Part II, pp. 87-106, 1976.
- [49] McQuiston, F.C., Parker, J.D., and Spitler, J.D., *Heating, ventilation, and air conditioning, Analysis and design*, 6th edition, Wiley & Sons, Hoboken, 2005.
- [50] Narayan, G.P., Private communication, Massachusetts Institute of Technology, Cambridge, MA, July 2010.

Table 1: Heat transfer correlations for parallel plate duct flow on the air side and the seawater side and for the condensate film

Fluid	Nusselt number correlation	Range, References
Air, seawater	$Nu_{l,z} = \left( Nu_{l,1}^3 + Nu_{l,z,2}^3 + Nu_{l,z,3}^3 \right)^{1/3}$ $Nu_{l,1} = 7.541$ $Nu_{l,z,2} = \frac{1.841}{2} (\text{Re Pr } D_h / z)^{1/3}$ $Nu_{l,z,3} = \frac{1}{2} \left( \frac{2}{1 + 22 \text{ Pr}} \right)^{1/6} (\text{Re Pr } D_h / z)^{1/2}$	Laminar flow Re < 2300, [40]
Air, seawater	$Nu_{t,z} = \frac{(\xi/8) \text{Re Pr}}{k_1 + 12.7 \sqrt{\xi/8} (\text{Pr}^{2/3} - 1)} \left[ 1 + \frac{1}{3} \left( \frac{d_h}{z} \right)^{2/3} \right] F_{ann}$ $k_1 = 1.07 + 900/\text{Re} - 0.63/(1 + 10 \text{ Pr})$ $\xi = (1.8 \lg(2/3 \text{ Re}) - 1.5)^{-2}$ $F_{ann} = 0.75 \text{ for parallel plate duct flow}$	Turbulent flow $10^4 < \text{Re} < 10^6$ $0.6 < \text{Pr} < 100$ , [41,42]
Air, seawater	$Nu_z = (1 - \gamma) Nu_{l,z,2300} + \gamma Nu_{t,z,10000}$ $\gamma = \frac{\text{Re} - 2300}{10^4 - 2300}$	Transition flow $2300 < \text{Re} < 10^4$ , [40-43]
Condensate	$h_{pw,z} = \frac{k_{pw}}{\delta} = \left( \frac{\rho_{pw} (\rho_{pw} - \rho_a) g h_{fg} k_{pw}^3}{4 \mu_{pw} (t_l - t_0)} \frac{1}{z} \right)^{1/4}$	Laminar condensate film [30]

Table 2: Plate length and width combination, heat transfer area, mean air velocity, mean seawater velocity, Reynolds number, air-side pressure drop, and specific heat transfer area which apply to the simulations shown in Figs. 8 to 10 for heat exchangers with an air-side plate spacing of 10 mm, and inlet conditions and heat flow from Fig. 6

	L m	W m	A m <sup>2</sup>	$\bar{w}_a$ m/s	$\bar{w}_{sw}$ m/s	Re <sub>a</sub>	$\Delta p_a$ Pa	A / $\dot{m}_{pw}$ m <sup>2</sup> /(kg/s)
+	2.36	8.11	38.28	8.52	0.054	4549	85.7	296.0
□	1.93	12.11	46.74	5.68	0.036	3037	32.6	362.6
∇	1.63	16.11	52.52	4.27	0.027	2283	16.3	408.2
*	1.32	20.11	52.94	3.42	0.022	1830	10.2	412.4
○	1.10	24.11	53.04	2.86	0.018	1526	7.1	
◇	0.98	27.11	53.14	2.54	0.016	1357	5.6	

Table 3: Plate length and width combination, heat transfer area, mean air velocity, mean seawater velocity, Reynolds number, air-side pressure drop, and specific heat transfer area which apply to the simulations for heat exchangers with an air-side plate spacing of 20 mm and 7 mm, and inlet conditions and heat flow from Fig. 6

$D_a$ mm	L m	W m	A $m^2$	$\bar{w}_a$ m/s	$\bar{w}_{sw}$ m/s	$Re_a$	$\Delta p_a$ Pa	$A/\dot{m}_{pw}$ , $m^2/(kg/s)$
20	5.00	4.06	40.48	8.51	0.108	9093	63.2	313.8
20	4.54	5.06	45.94	6.82	0.086	7283	37.6	356.0
20	4.22	6.06	51.12	5.68	0.072	6072	24.7	397.0
20	3.98	7.06	56.16	4.87	0.062	5206	17.4	436.7
20	3.79	8.06	61.06	4.26	0.054	4555	12.9	474.9
20	3.62	9.06	65.56	3.78	0.048	4049	9.8	510.7
20	3.48	10.06	69.98	3.40	0.043	3643	7.7	545.4
20	3.36	11.06	74.30	3.09	0.039	3311	6.2	579.0
20	3.25	12.06	78.36	2.83	0.036	3035	5.1	610.9
20	3.14	13.06	82.00	2.62	0.033	2801	4.2	640.1
20	3.05	14.06	85.74	2.43	0.031	2600	3.6	669.3
7	1.58	11.59	36.62	8.48	0.038	3174	99.8	283.2
7	1.51	12.59	38.02	7.80	0.035	2920	81.4	294.1
7	1.47	13.59	39.95	7.22	0.032	2701	68.4	307.4
7	1.39	14.59	40.56	6.72	0.030	2517	56.6	313.4
7	1.32	15.59	41.15	6.30	0.028	2357	48.0	318.8
7	1.26	16.59	41.80	5.92	0.026	2216	41.7	323.2
7	0.50	41.59	41.59	2.36	0.010	884	6.5	322.3



## LIST OF FIGURES

Figure 1: System architecture of a closed-air open-water water-heated humidification-dehumidification (HDH) desalination system

Figure 2: Top: Discretized plate dehumidifier with marked control volume (cell). Below: Control volume in the dehumidifier showing variables used, boundary layer temperature distribution in seawater, condensate and humid air near the plate surface, and partial pressures in the humid air

Figure 3: Sensitivity of the plate heat exchanger model to the number of cells in flow direction for the given parameters. Results indicate the change of quantities relative to the simulation with 10 fewer cells

Figure 4: Comparison of different heat transfer correlations with McQuiston's [48] experimental data

Figure 5: Comparison of experimental data for dehumidification (series 3000) [48] with simulations from the plate heat exchanger model. The maximum deviation  $\varepsilon$  between experiment and simulation is given for the humidity ratio change, the heat flow, the air temperature change and the cooling water temperature change. To show the effect of the experimental humidity ratio errors in the experiments, the numerical results for simulation with  $\pm 1$  g/kg are also presented

Figure 6: Inlet and outlet conditions at the operating point of the dehumidifier [50] with  $t_{swI}$  adjusted for seawater operation

Figure 7: Temperature distribution, humidity ratio distribution and mass flow of product water for different heat exchanger lengths with plate width 12.11 m, air-side plate spacing 10 mm, and inlet conditions from Fig. 6

Figure 8: Temperature distribution in heat exchangers of plate length and width combinations according to Table 2, with air-side plate spacing 10 mm, and inlet conditions and heat flow from Fig. 6

Figure 9: Humidity ratio distribution and product water mass flow in heat exchangers of plate length and width combinations according to Table 2, with air-side plate spacing 10 mm, and inlet conditions and heat flow from Fig. 6

Figure 10: Air flow velocity, Reynolds number and air-side heat transfer coefficient in heat exchangers of plate length and width combinations according to Table 2, with air-side plate spacing 10 mm, and inlet conditions and heat flow from Fig. 6

Figure 11: Air-side pressure drop in heat exchangers with air-side plate spacings of  $D_a = 7$  mm, 10 mm and 20 mm for plate length and width combinations for the inlet conditions and the heat flow from Fig. 6

Figure 12: Air, product water and seawater outlet temperature, outlet humidity ratio, product water mass flow, heat flow and air-side pressure drop as a function of plate thermal conductivity for 0.7 mm thick plates (bottom scale) and as a function of plate thickness for plates with a thermal conductivity of 1 W/(m K) (top scale) for a heat exchanger with plates of 1.93 m length and 12.11 m width, air-side plate spacing of  $D_a = 10$  mm, and inlet conditions from Fig. 6

Figure 13: Air, product water and seawater outlet temperatures, outlet humidity ratio, product water mass flow, heat flow and air-side pressure drop as functions of the seawater-side plate spacing for a heat exchanger with magnetite-filled PP plates of 1.93 m length, 12.11 m width and 0.7 mm thickness, an air-side plate spacing of  $D_a = 10$  mm, and inlet conditions as for the operating point of Fig. 6

Figure 14: Air outlet temperature for heat exchangers with different plate lengths and widths as a function of heat transfer area and air-side pressure drop for air-side plate spacing 10 mm, and inlet conditions from Fig. 6. The mesh indicates constant length  $L$  and constant width  $W$ . The dashed white line represents  $Re_a = 2300$ . The geometries for the operating point in Fig. 6 with 10 mm air-side plate spacing are located on the gray line for  $\dot{Q}=169\text{kW}$

Figure 15: Heat flow for heat exchangers with different plate lengths and widths as a function of heat transfer area and air-side pressure drop for air-side plate spacing 10 mm, and inlet conditions from Fig. 6. The mesh indicates constant length  $L$  and constant width

W. The dashed white line represents  $Re_a = 2300$ . The geometries for the operating point in Fig. 6 with 10 mm air-side plate spacing are located on the gray line for  $\dot{Q}=169\text{ kW}$

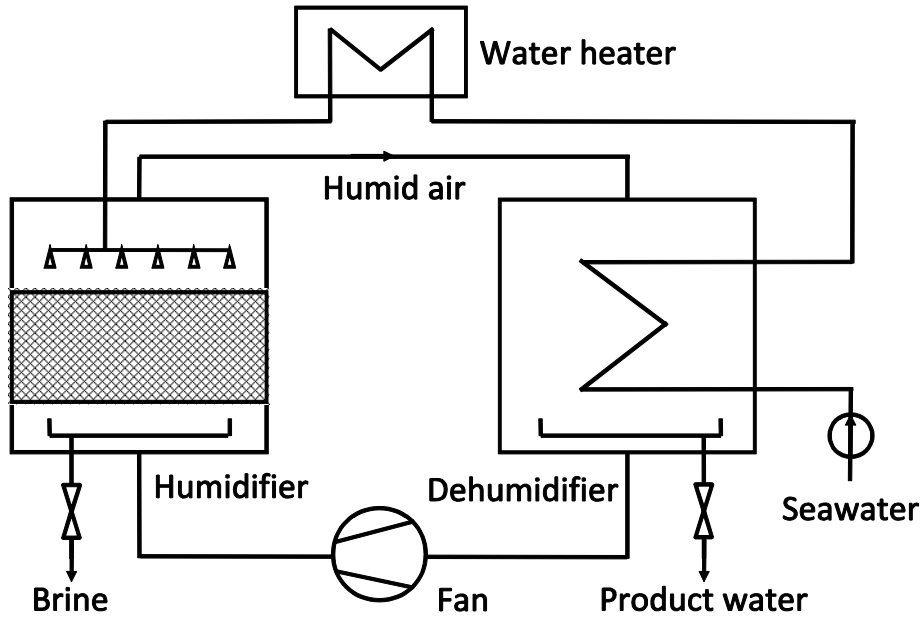


Figure 1: System architecture of a closed-air open-water water-heated humidification-dehumidification (HDH) desalination system

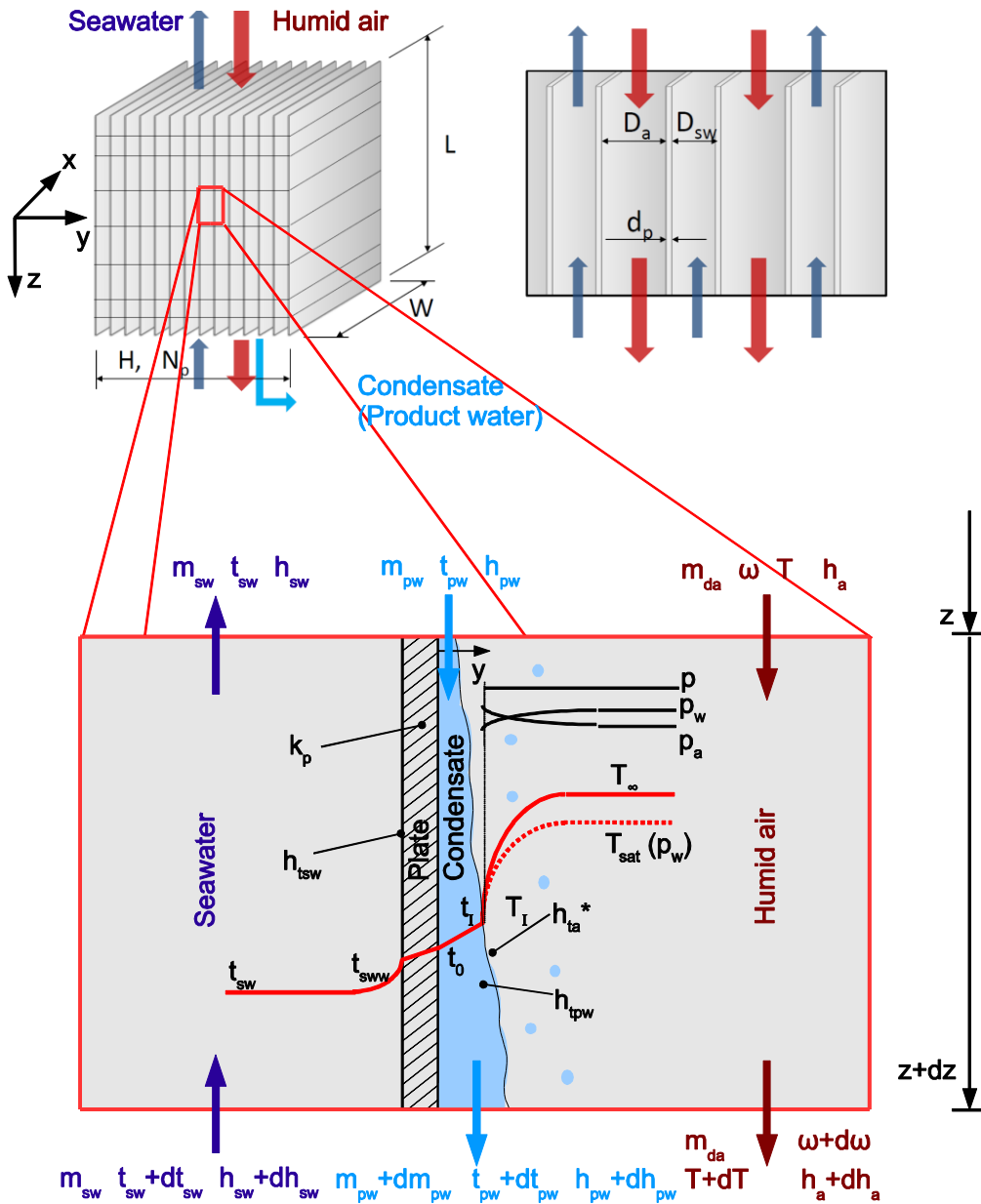


Figure 2: Top: Discretized plate dehumidifier with marked control volume (cell). Below: Control volume in the dehumidifier showing variables used, boundary layer temperature distribution in seawater, condensate and humid air near the plate surface, and partial pressures in the humid air

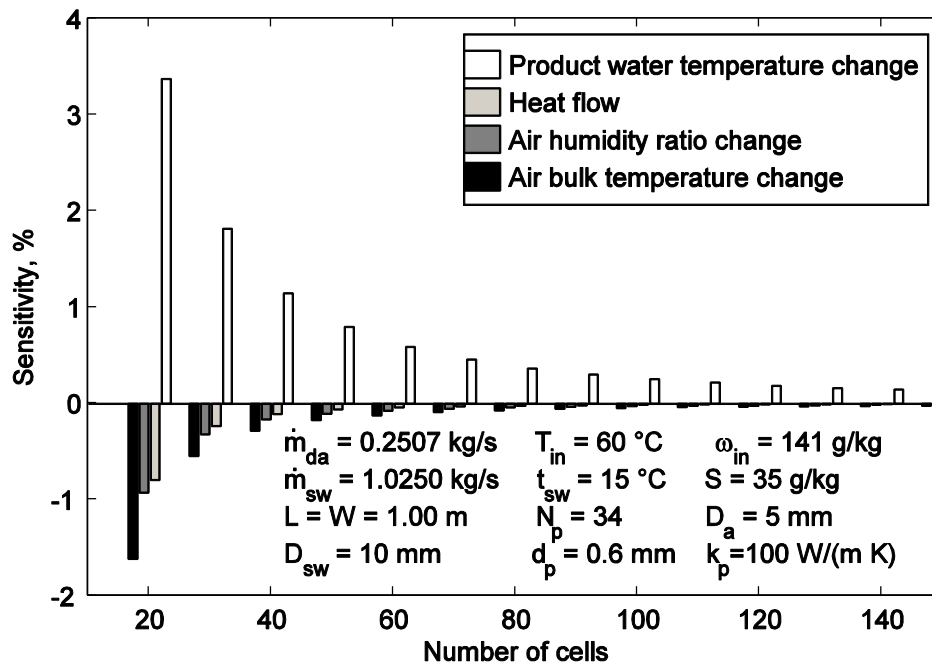


Figure 3: Sensitivity of the plate heat exchanger model to the number of cells in flow direction for the given parameters. Results indicate the change of quantities relative to the simulation with 10 fewer cells

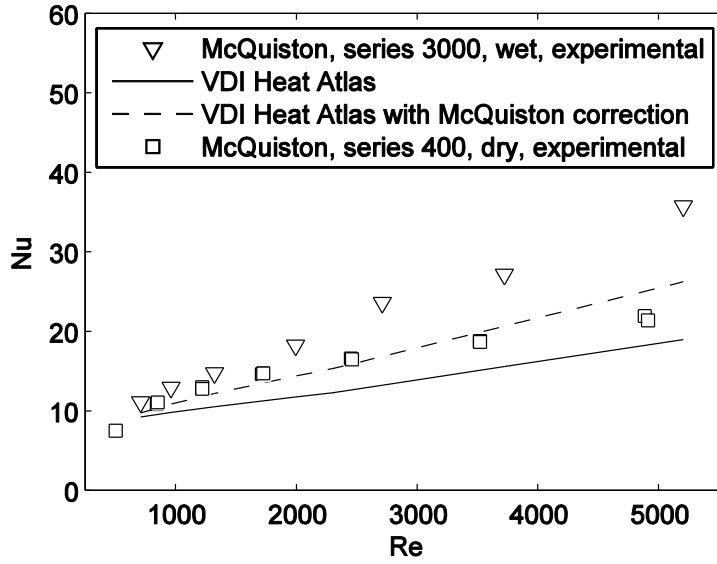


Figure 4: Comparison of different heat transfer correlations with McQuiston's [48] experimental data

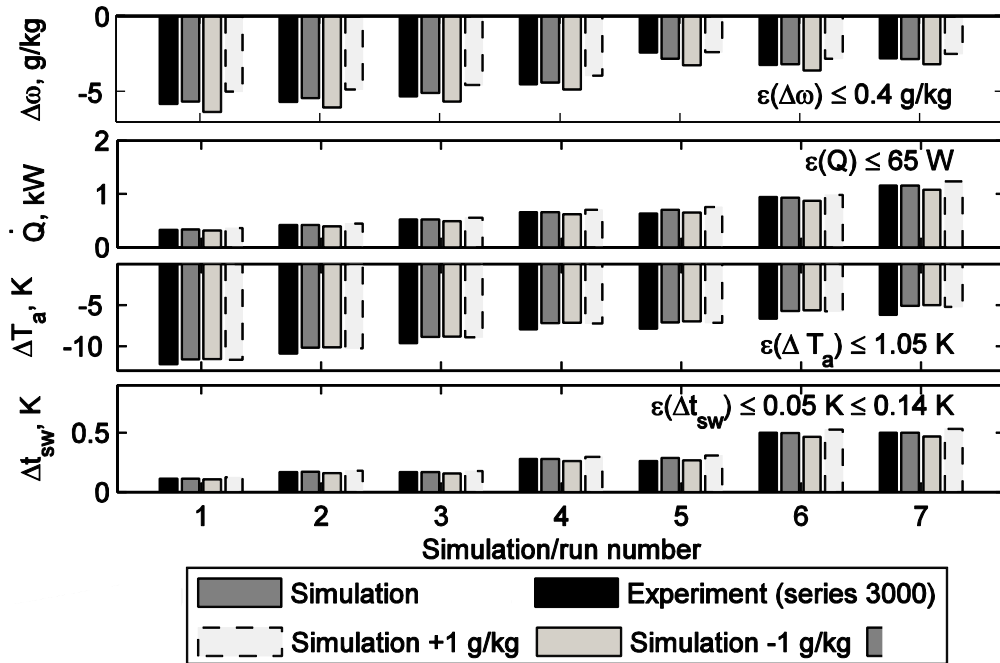


Figure 5: Comparison of experimental data for dehumidification (series 3000) [48] with simulations from the plate heat exchanger model. The maximum deviation  $\varepsilon$  between experiment and simulation is given for the humidity ratio change, the heat flow, the air temperature change and the cooling water temperature change. To show the effect of the experimental humidity ratio errors in the experiments, the numerical results for simulation with  $\pm 1$  g/kg are also presented



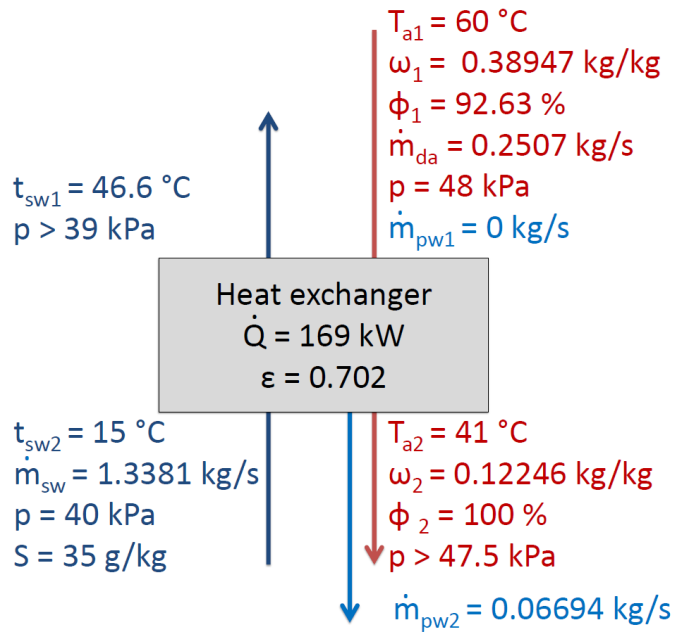


Figure 6: Inlet and outlet conditions at the operating point of the dehumidifier [50] with  $t_{sw1}$  adjusted for seawater operation

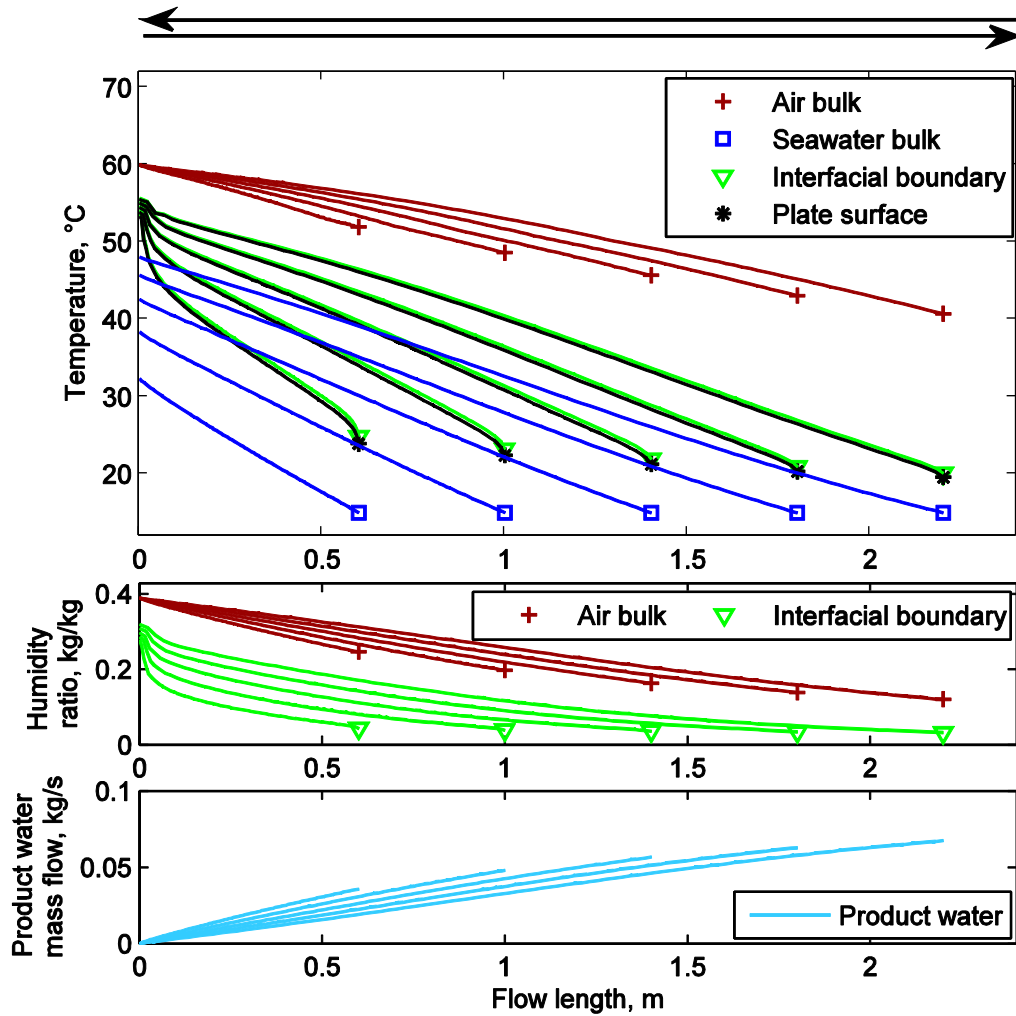


Figure 7: Temperature distribution, humidity ratio distribution and mass flow of product water for different heat exchanger lengths with plate width 12.11 m, air-side plate spacing 10 mm, and inlet conditions from Fig. 6

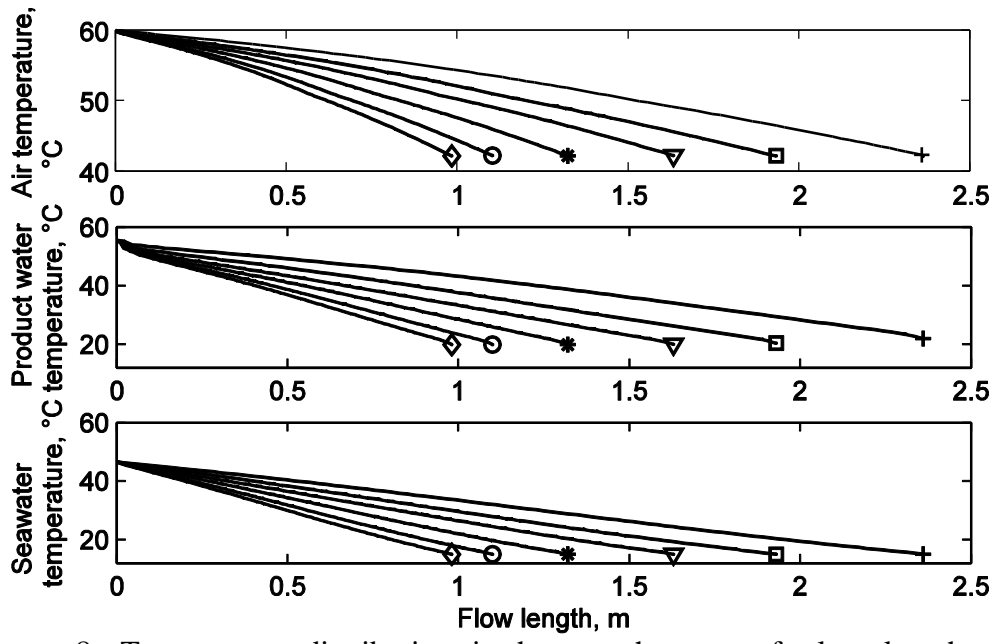


Figure 8: Temperature distribution in heat exchangers of plate length and width combinations according to Table 2, with air-side plate spacing 10 mm, and inlet conditions and heat flow from Fig. 6

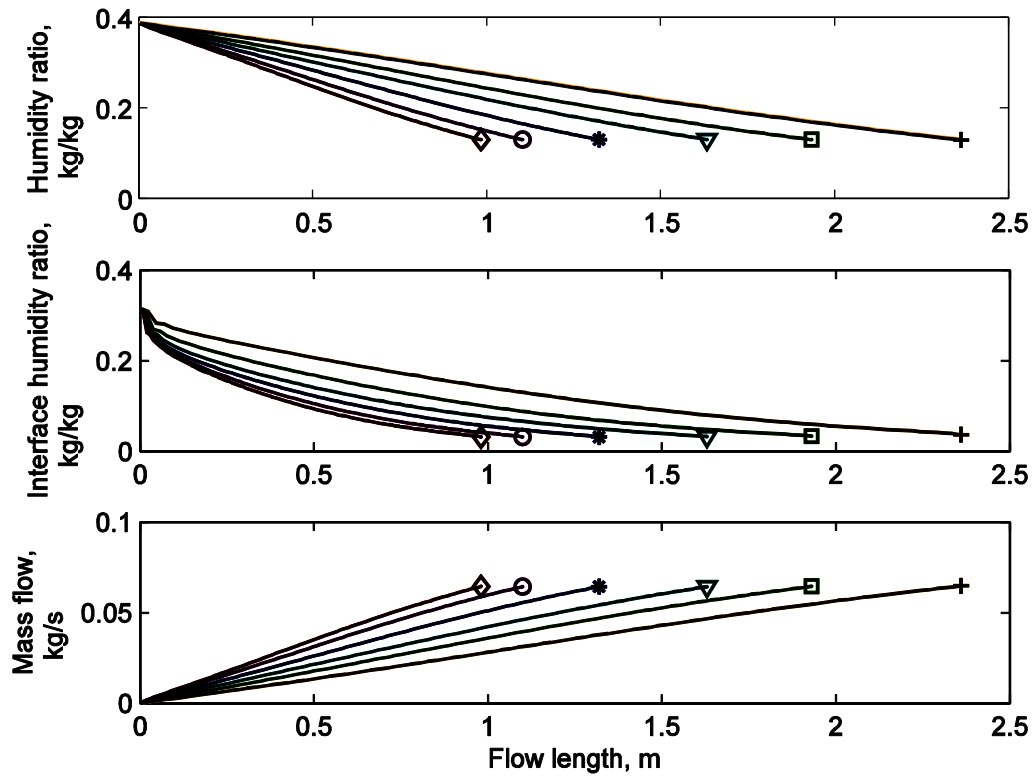


Figure 9: Humidity ratio distribution and product water mass flow in heat exchangers of plate length and width combinations according to Table 2, with air-side plate spacing 10 mm, and inlet conditions and heat flow from Fig. 6

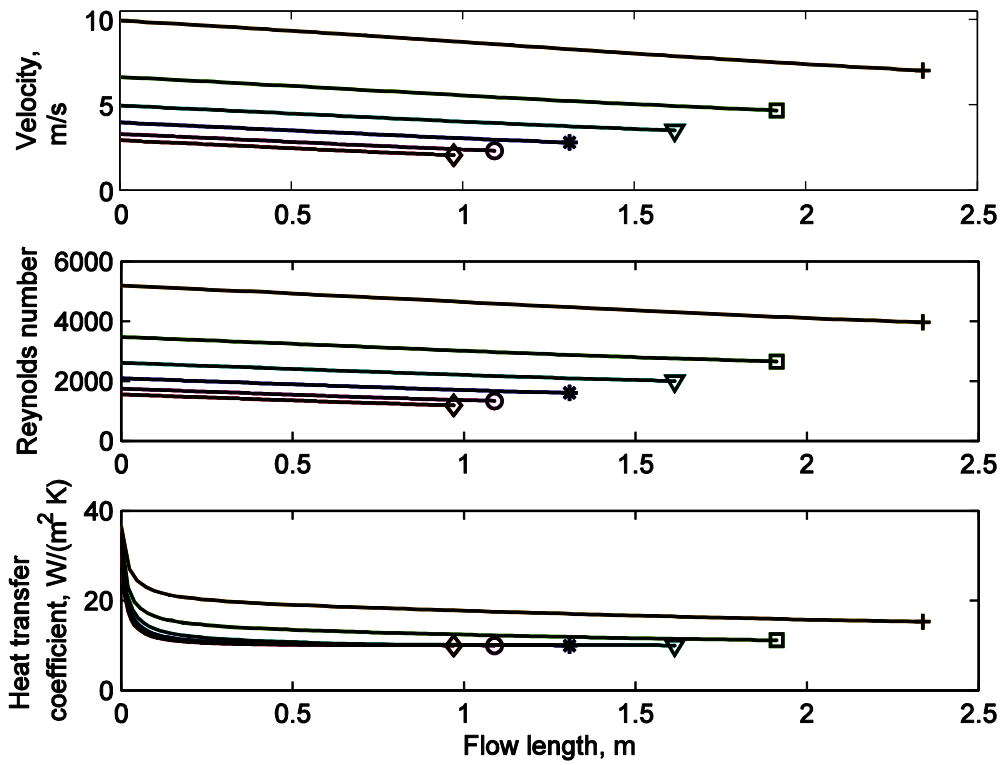


Figure 10: Air flow velocity, Reynolds number and air-side heat transfer coefficient in heat exchangers of plate length and width combinations according to Table 2, with air-side plate spacing 10 mm, and inlet conditions and heat flow from Fig. 6

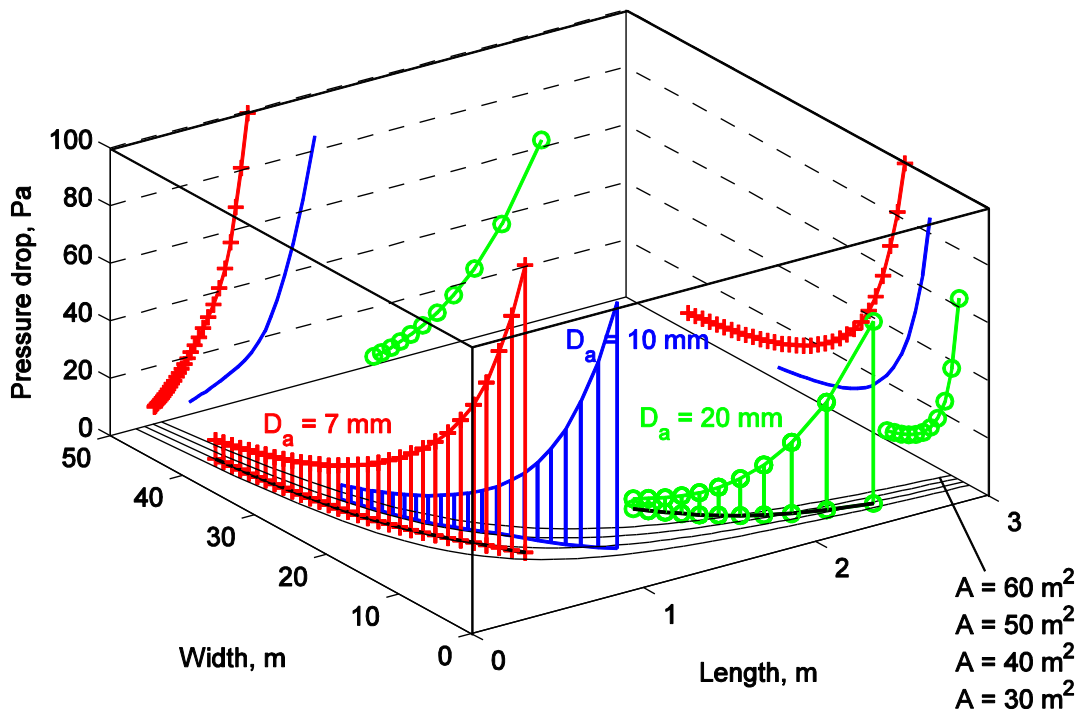


Figure 11: Air-side pressure drop in heat exchangers with air-side plate spacings of  $D_a = 7$  mm, 10 mm and 20 mm for plate length and width combinations for the inlet conditions and the heat flow from Fig. 6

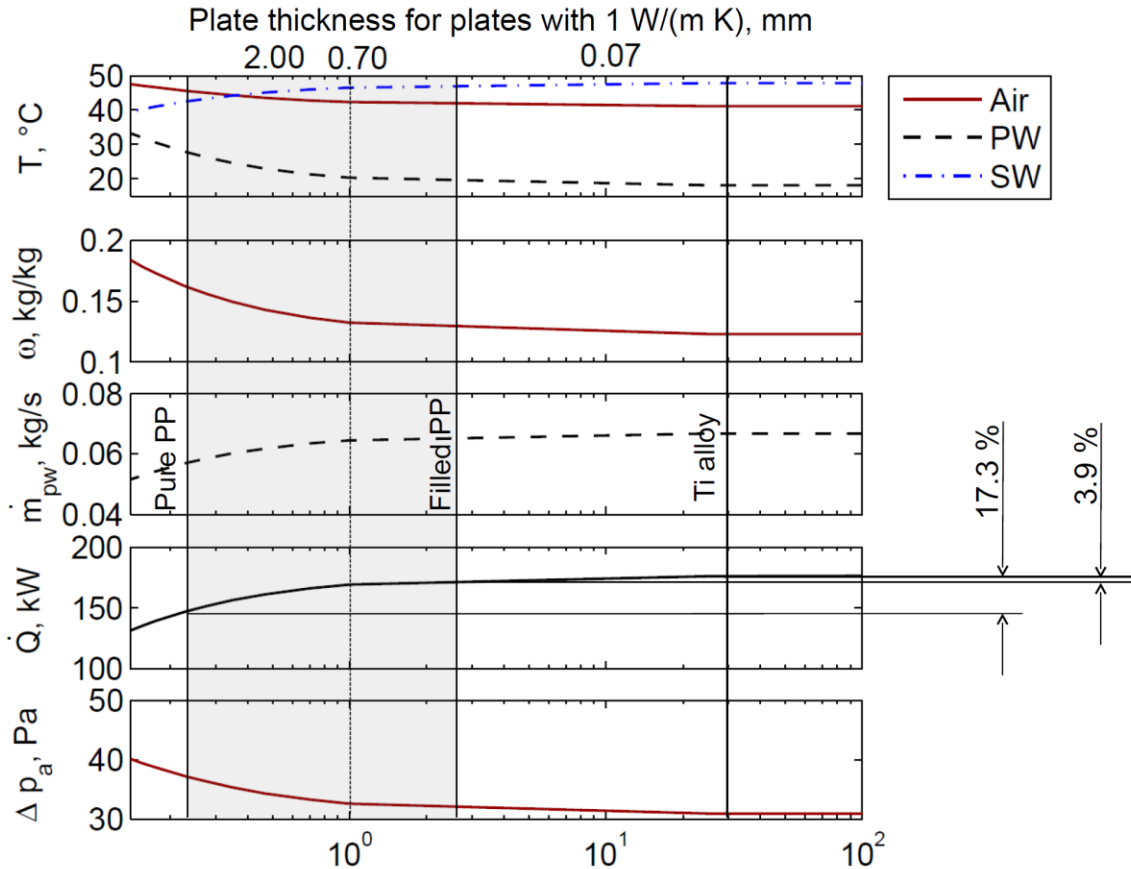


Plate thermal conductivity with 0.7 mm thick plates, W/(m K)

Figure 12: Air, product water and seawater outlet temperature, outlet humidity ratio, product water mass flow, heat flow and air-side pressure drop as a function of plate thermal conductivity for 0.7 mm thick plates (bottom scale) and as a function of plate thickness for plates with a thermal conductivity of 1 W/(m K) (top scale) for a heat exchanger with plates of 1.93 m length and 12.11 m width, air-side plate spacing of  $D_a = 10$  mm, and inlet conditions from Fig. 6

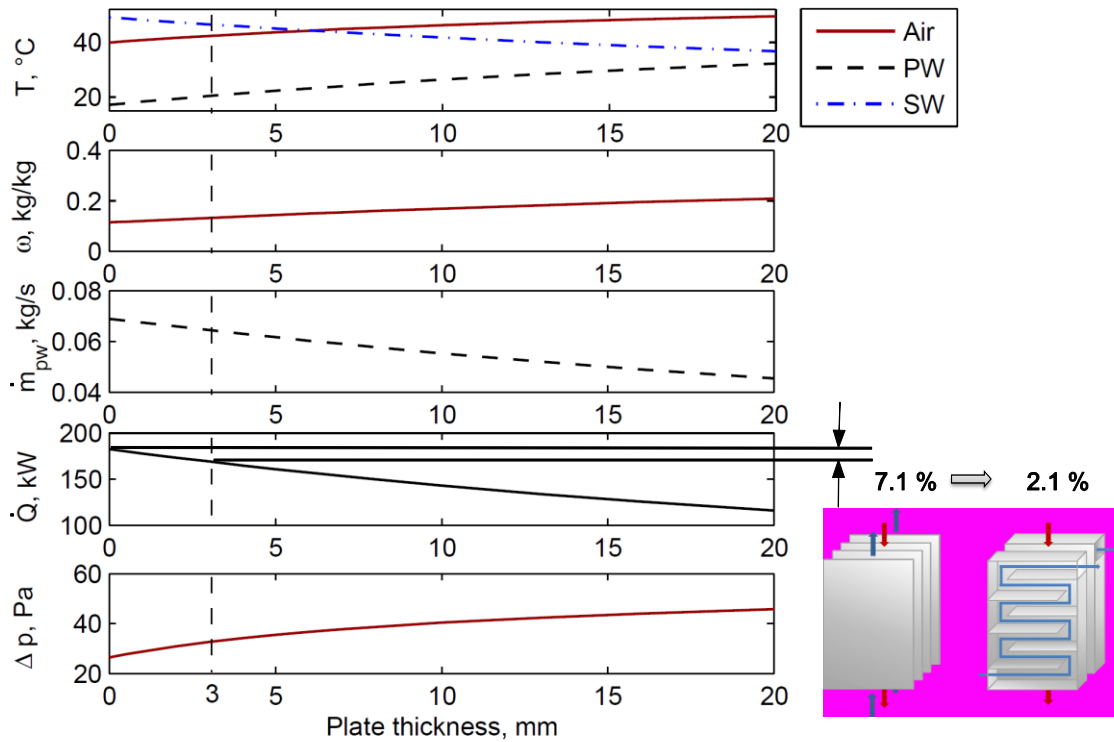


Figure 13: Air, product water and seawater outlet temperatures, outlet humidity ratio, product water mass flow, heat flow and air-side pressure drop as functions of the seawater-side plate spacing for a heat exchanger with magnetite-filled PP plates of 1.93 m length, 12.11 m width and 0.7 mm thickness, an air-side plate spacing of  $D_a = 10$  mm, and inlet conditions as for the operating point of Fig. 6



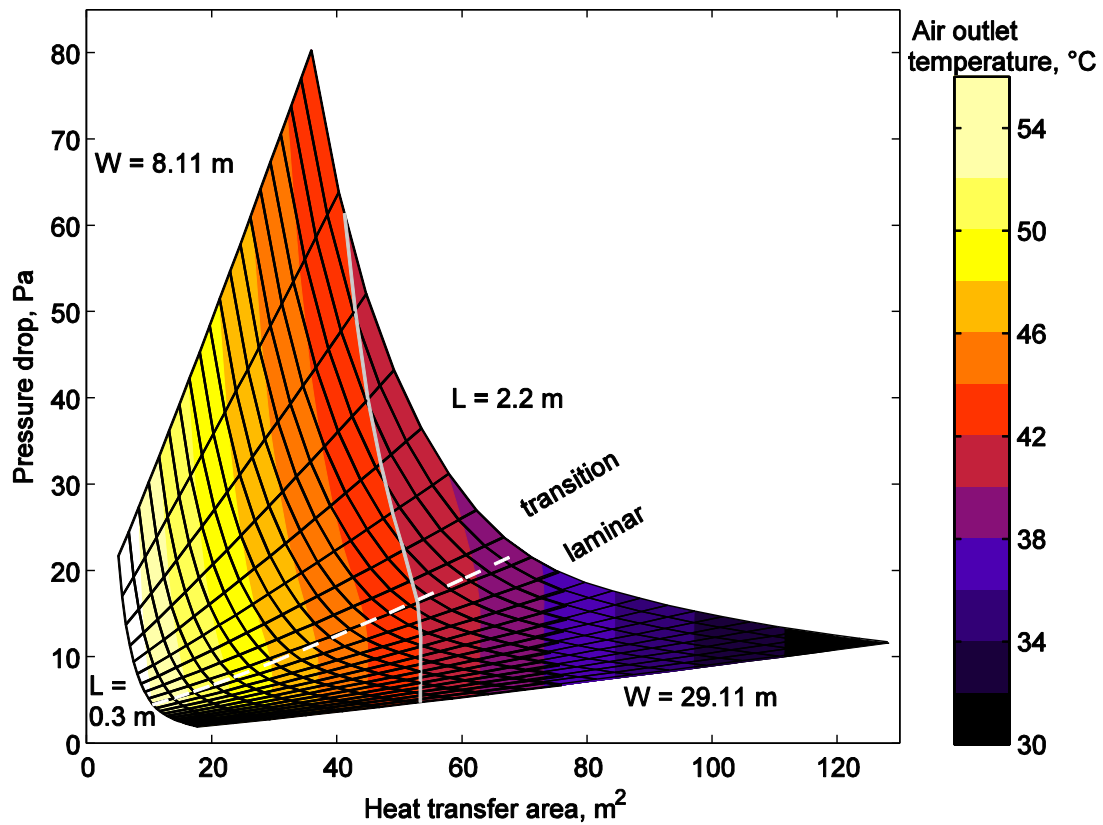


Figure 14: Air outlet temperature for heat exchangers with different plate lengths and widths as a function of heat transfer area and air-side pressure drop for air-side plate spacing 10 mm, and inlet conditions from Fig. 6. The mesh indicates constant length  $L$  and constant width  $W$ . The dashed white line represents  $Re_a = 2300$ . The geometries for the operating point in Fig. 6 with 10 mm air-side plate spacing are located on the continuous gray line for  $\dot{Q}=169\text{ kW}$

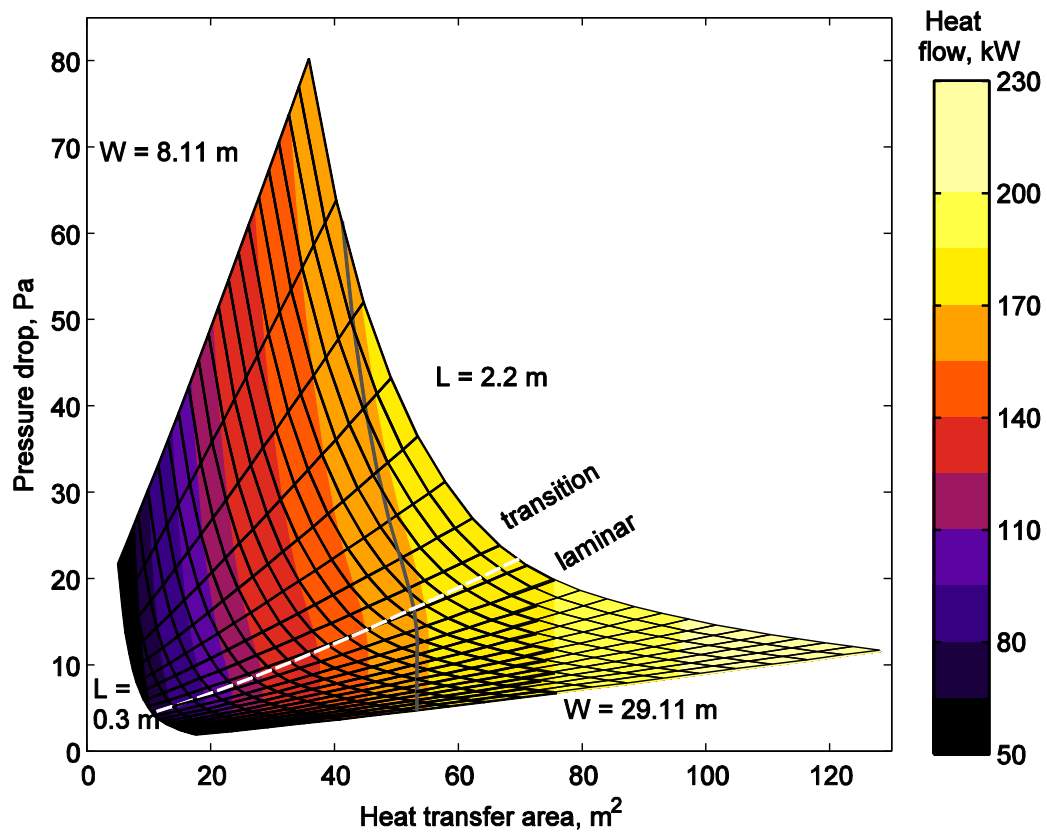


Figure 15: Heat flow for heat exchangers with different plate lengths and widths as a function of heat transfer area and air-side pressure drop for air-side plate spacing 10 mm, and inlet conditions from Fig. 6. The mesh indicates constant length  $L$  and constant width  $W$ . The dashed white line represents  $Re_a = 2300$ . The geometries for the operating point in Fig. 6 with 10 mm air-side plate spacing are located on the continuous gray line for  $\dot{Q} = 169 \text{ kW}$



Martin Sievers is a doctoral student at Stuttgart University, Germany. He obtained a B. Sc. in General Engineering Science and a Dipl.-Ing. in Mechanical Engineering from Hamburg University of Technology, Germany. In 2008/09 he was a visiting graduate student in the Department of Mechanical Engineering at the University of California at Berkeley and in 2010 in the Department of Mechanical Engineering at Massachusetts Institute of Technology. His research interests are power electronics cooling, heat exchanger design, and fluid dynamics of multi-component mixtures involving heat and mass transfer.



John H. Lienhard V is the Collins Professor of Mechanical Engineering at MIT. During more than 24 years on the MIT faculty, Lienhard's research and educational efforts have focused on heat transfer, desalination, thermodynamics, fluid mechanics, and instrumentation. He has also filled a number of administrative roles at MIT. Lienhard received his bachelors and masters degrees in thermal engineering at UCLA from the Chemical, Nuclear, and Thermal Engineering Department, and his PhD from the Applied Mechanics and Engineering Science Department at UC San Diego. He has been the Director of the Rohsenow Kendall Heat Transfer Laboratory since 1997, and he is the Director of the Center for Clean Water and Clean Energy at MIT and KFUPM.